JOURNAL OF STRUCTURAL BIOLOGY **118,** 197–219 (1997)
ARTICLE NO. SB973845

Three-Dimensional Reconstruction with Contrast Transfer Function Correction from Energy-Filtered Cryoelectron Micrographs: Procedure and Application to the 70S *Escherichia coli* Ribosome

Jun Zhu

Wadsworth Center, New York State Department of Health, Empire State Plaza, P.O. Box 509, Albany, New York 12201-0509; and Department of Biomedical Sciences, School of Public Health, State University of New York at Albany, Empire State Plaza, P.O. Box 509, Albany, New York 12201-0509

Pawel A. Penczek

Wadsworth Center, New York State Department of Health, Empire State Plaza, P.O. Box 509, Albany, New York 12201-0509

Rasmus Schröder

Department of Biophysics, Max-Planck Institute for Medical Research, Jahnstrasse 29, 69120 Heidelberg, Germany

and

Joachim Frank[1]

Wadsworth Center, New York State Department of Health, Empire State Plaza, P.O. Box 509, Albany, New York 12201-0509; and Department of Biomedical Sciences, School of Public Health, State University of New York at Albany, Empire State Plaza, P.O. Box 509, Albany, New York 12201-0509

Received September 12, 1996, and in revised form January 6, 1997

Cryoelectron microscopy provides the means of studying macromolecules in their native state. However, the contrast transfer function (CTF) makes the images and the three-dimensional (3D) maps derived from them difficult to interpret. We developed methods to determine the CTF from experimental data and to obtain a CTF-corrected 3D reconstruction. The CTF correction and 3D reconstruction accomplished in one step make it easy to combine different defocus data sets and decrease the error accumulation in the computation. These methods were applied to energy-filtered images of the 70S *Escherichia coli* ribosome, resulting in a distortion-free 3D map of the ribosome at 1/24.5 Å^{-1} resolution, as determined by the differential phase residual resolution criterion.

[1] To whom correspondence should be addressed at Wadsworth Center, New York State Department of Health, Empire State Plaza, P.O. Box 509, Albany, NY 12201-0509. Fax: (518) 486-2191; E-mail: joachim@wadsworth.org.

1. INTRODUCTION

Electron microscopy (EM) played a key role in the discovery of the ribosome (Palade, 1955) and it is still the main tool for studying its structure. It has been difficult to grow ribosome crystals that are sufficiently well ordered and large for analysis by electron or X-ray crystallography. Due to recent advances in cryo-EM, noncrystallographic image processing and three-dimensional (3D) reconstruction techniques (Radermacher *et al.*, 1987; van Heel, 1987; Frank *et al.*, 1988a,b; Penczek *et al.*, 1992, 1994) it has become possible to form 3D images of the ribosome at a resolution that allows the study of functional states.

To achieve high resolution in a 3D reconstruction of biological molecules using EM, the specimen structure must be well preserved. Methods of preserving and imaging biological molecules in thin layers of vitreous ice (Lepault *et al.*, 1983) have created new possibilities for quantitative EM. Bright-field imaging of frozen-hydrated specimens has emerged as a reliable high-resolution technique for examining molecules in their native hydrated state.

1047-8477/97 $25.00

To a good approximation the intensity observed in an EM bright-field image is a projection of the 3D Coulomb potential distribution corrupted by the wave aberrations of the objective lens. Image contrast is formed by interference of scattered and unscattered electron waves (Hanszen, 1971). Formally, the relationship between object density and image contrast is described by the contrast transfer theory (see review by Wade, 1992). According to this theory, the Fourier transform of the bright-field image is related to the Fourier transform of the object's Coulomb potential by multiplication with the electron microscope's contrast transfer function (CTF), whose precise spatial frequency dependence is controlled by the defocus setting. Since the spatial frequencies originally present in the object are not represented equally in the image, the interior features and boundaries of the molecule may be altered substantially, making it difficult to interpret the image without CTF correction. The successes of the negative stain technique can be explained by the fact that staining introduces amplitude contrast which largely makes up for the reduction in phase contrast that occurs at low frequencies (Erickson and Klug, 1970). A compensation for the effect of the CTF becomes essential for unstained, ice-embedded specimens. In the absence of heavy metal salts, the amplitude contrast has only a weak effect and the image contrast is strongly diminished (Stewart and Vigers, 1986). Attempts to reconstruct the correct object are hampered by the presence of inelastic scattering, which produces a component of the image that does not follow the contrast transfer theory. Through the use of an energy-filtered electron microscopy this component can be eliminated, resulting in an image that strictly obeys the CTF theory.

In practice, the limit on the resolution that can be achieved by the EM is set by the position of the first zero of the CTF, which is determined by the defocus used. Substantial increase of the resolution can be accomplished only by collecting data from a defocus series. If the defocus values are chosen in such a way that the zeros of the corresponding CTFs do not coincide, it becomes possible to combine the data sets and extend the resolution beyond the first zero of the CTF. This correction can be applied either on the level of the raw data, by combining differently defocused micrographs (Schiske, 1973; Typke *et al.*, 1992), or, more effectively, on the level of reconstructed volumes, which as a result of averaging over many projections have a high signal-to-noise ratio (Langmore and Smith, 1992; Schröder *et al.*, 1993; Frank and Penczek, 1995). The disadvantage shared by both approaches is that they require two steps for the final volume to be obtained, causing an unnecessary accumulation of errors. Here we present a method of 3D reconstruction that includes the CTF correction and thus allows the final volume to be obtained in a single step. The elimination of the second step is expected to improve both the numerical accuracy and the resolution of the results. The CTF parameters, required by the 3D reconstruction program, are retrieved from the experimental data. The results obtained by applying these new methods to energy-filtered cryoimages of the ribosome have been published recently (Frank *et al.*, 1995a,b).

2. METHODS

2.1 Role of Energy Filtration

Images of frozen-hydrated, biological specimens have low contrast because the densities of biological matter and the surrounding vitreous ice are similar. The images also contain a high background caused by inelastic scattering. When electrons with 100 keV energy pass a thin (500–1000 Å) ice layer, in which the macromolecule specimen is embedded, at least 50% percent of the scattered electrons undergo inelastic scattering processes (Schröder *et al.*, 1990; Langmore and Smith, 1992; Angert *et al.*, 1996) and more than 30% of the scattered electrons undergo multiple scattering processes (Angert *et al.*, 1996). Inelastically scattered electrons cannot interfere with the primary beam, so they give no phase contrast. Inelastic scattering is concentrated at very small angles so that almost all the electrons that have been inelastically scattered are focused into the image and do not give rise to scattering contrast, a component of the contrast that is generated by electrons scattered at large angles and removed by the objective aperture (Langmore and Smith, 1992). Thus, inelastic scattering generates no meaningful contrast, but only contributes a high, slowly varying background to the image. In addition, if multiple scattering events do occur, the inelastically scattered electrons can give rise to elastic bright-field images, and the image we observe can be thought of as a superposition of a large number of bright-field images, each originating from an inelastically scattered electron having different angular incidence and energy (Reimer and Ross-Messemer, 1990).

Introduction of energy filtration reduces many of the problems described. Through elimination of inelastically scattered electrons, energy-filtered cryo-EM increases the contrast and yields improved structural resolution (Schröder *et al.*, 1990). A comparison of filtered and unfiltered images and their power spectra at the same defocus is shown in Fig. 1. As the number of electrons that reach the emulsion are different, the power spectra of energy-filtered and unfiltered images have different scales, making a normalization step necessary. Assuming that the value at medium spatial frequencies are the same in both energy-filtered and unfiltered power spectra, we normalized the two power spectra so that the first peak has the same height, as shown in Fig. 2a. After elimination of the noise background, which is similar in both spectra, the power spectrum of the unfiltered image is distinguished from that of the filtered image by a high peak at low spatial frequencies that must be attributed to image components due to small-angle inelastically scattered electrons, as shown in Fig. 2b. To see the behavior at high spatial frequencies more clearly, we masked out the low-frequency peaks and boosted the scale, as shown in Fig. 2c. The fact that the value of the unfiltered power spectrum at high spatial frequencies is lower than that in the filtered one can be explained by the multiple scattering effects mentioned above. However, this falloff could also be explained as an effect of radiation damage since the energy-filtered image was taken first and the unfiltered one second. This alternative explanation can be eliminated on the basis of two experimental observations: (i) there is no obvious falloff at high spatial frequency among the power spectra in the defocus series (not shown here); (ii) if pairs of energy-filtered and unfiltered TMV images taken in both orders are compared, there is not significant difference (Angert

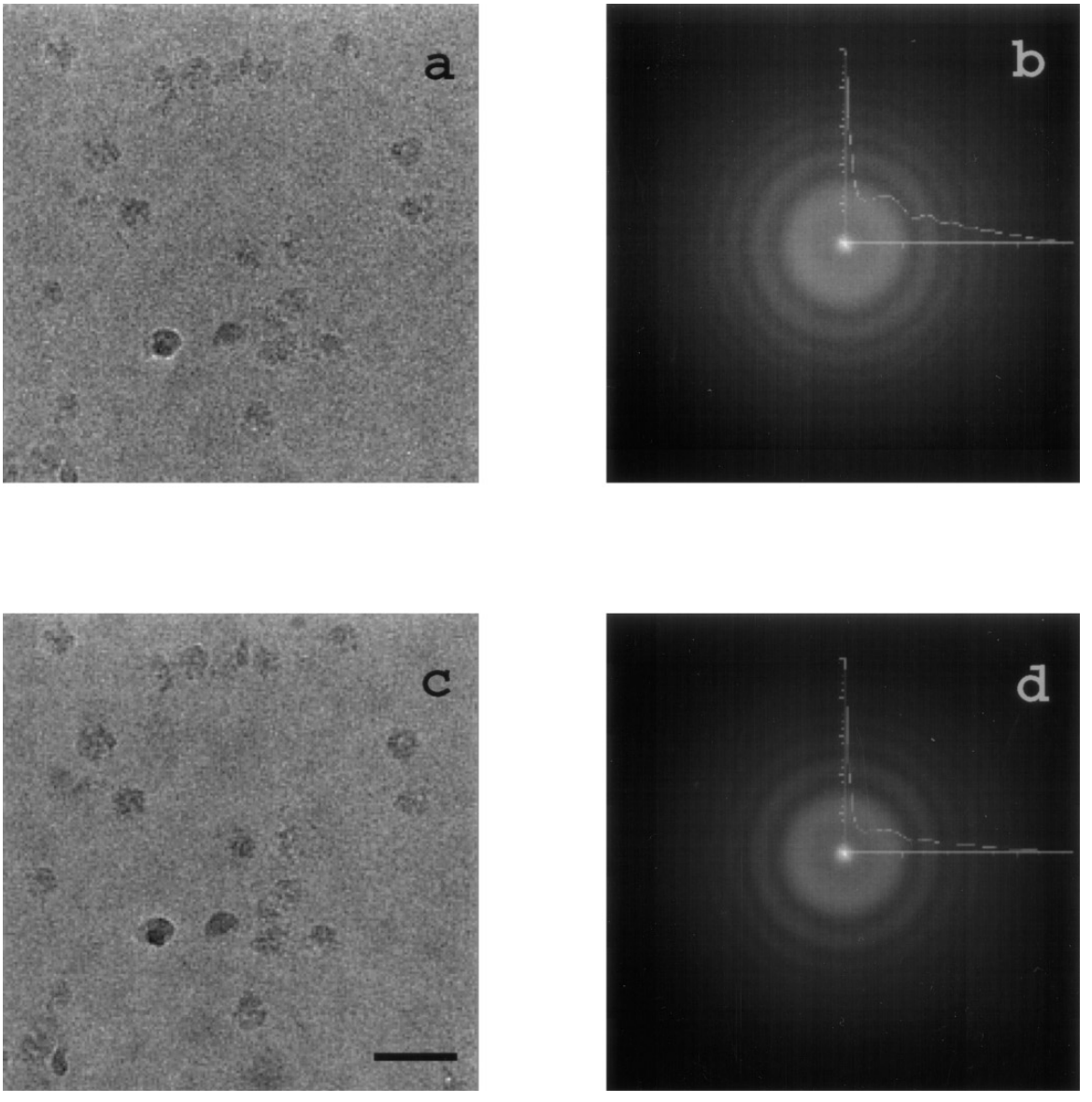

FIG. 1. Effect of energy filtration on power spectrum. The same area of the specimen was exposed at the same defocus under low-dose conditions with and without energy filter in place. The energy-filtered image was recorded first. The electron dose for each exposure was $5e^{-}/Å^2$. The energy window width was 14eV, and the magnification ×52 000. (a) A cryoimage with energy filtration; the contrast is 4.0×10^{-3}; (b) the corresponding power spectrum of (a); the insert is the rotational average of the power spectrum; (c) image of the same area of the specimen as (a) but without energy filtration; the contrast is 3.68×10^{-3}; (d) the corresponding power spectrum of (c); the insert is the rotational average. Definitions used:

$$\text{contrast} = \frac{1}{I * J - 1} \sum_{i=1}^{I} \sum_{j=1}^{J} [p_{ij} - \langle p \rangle]^2,$$

where (p) is the average,

$$\langle p \rangle = \frac{1}{I * J} \sum_{i=1}^{I} \sum_{j=1}^{J} p_{ij}, \; p_{ij}$$

is the pixel value at position i and j, I and J are the dimensions of the image field. The length of the scale bar corresponds to 500 Å. The maximum spatial frequency for (b) and (d) is $1/7.6\ Å^{-1}$.

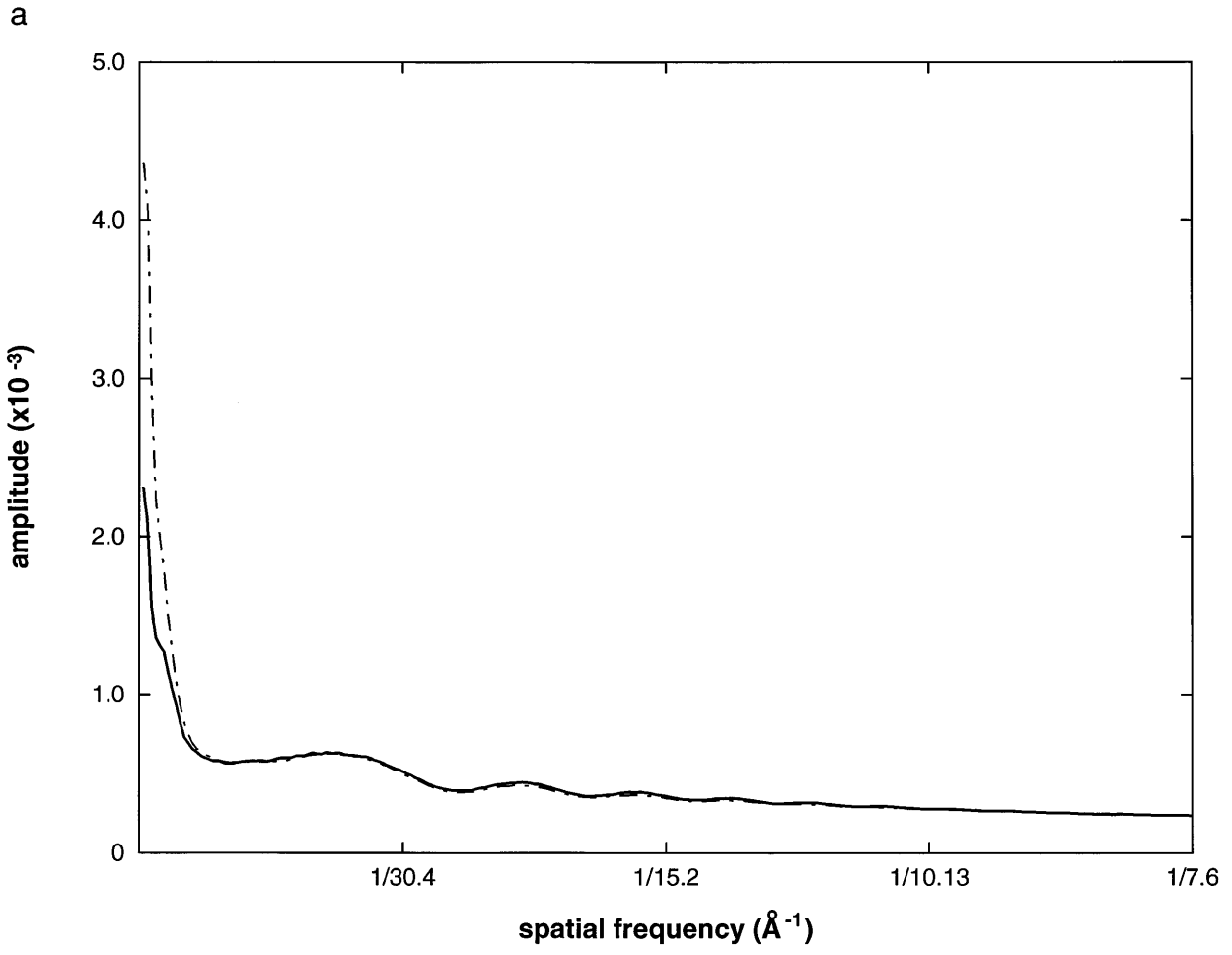

FIG. 2. Comparison of power spectra for energy-filtered and unfiltered images. The two power spectra are normalized so that the first peaks in the rotationally averaged 1D profiles have the same heights. The solid line is the 1D profile of the energy-filtered power spectrum, and the dashed line is the unfiltered one. The power spectrum of the unfiltered image has a higher low-spatial-frequency peak than the energy-filtered one due to the contribution by inelastic scattering, while its values at high spatial frequencies are reduced due to a multiple scattering effect. (a) Normalized 1D profiles; (b) 1D profiles with background subtracted; (c) 1D profiles of (b) displayed with enhanced scale. The amplitude is in arbitrary units.

and Schröder, unpublished data). Thus we conclude that for our specimens and for similar biological specimens, radiation damage is not an important factor in the observed high spatial frequency decrease in the power spectrum of the unfiltered image. Simulated energy-filtered and unfiltered images using Dinges' program (Dinges *et al.*, 1995) also show a similar decrease in high frequencies in unfiltered images.

Correction of EM images for the effects of the CTF usually follows a linear model, as derived from weak-phase approximation which holds only for elastic scattering. As inelastic scattering dominates the low spatial frequencies of cryo-EM images, such compensation of the CTF will overemphasize low-resolution features of the object. Again, the only way to solve this problem is to use energy-filtered EM in the zero energy loss mode where virtually all inelastically scattered electrons are eliminated. Elastic scattering from nucleic acids is predicted to be more than twice as strong as that from protein, whereas inelastic scattering is similar for the two types of molecules (Smith and Langmore, 1992). Thus, energy filtration should also greatly increase the contrast between RNA and protein (Smith and Langmore, 1992), a desired effect in the study of the ribosome. Finally, by combining energy-filtered cryo-EM with CTF correction one can, in principle, obtain absolute densities of biological molecules that agree very well with those from X-ray structures (Langmore and Smith, 1992; Schröder *et al.*, 1993).

2.2 Accurate Retrieval of CTF from Micrographs

In transmission electron microscopy, the scattering interaction of electron with object is depicted as a phase shift of the incoming wave $\tau_{in}(\mathbf{r})$:

$$\tau_{out}(\mathbf{r}) = \tau_{in}(\mathbf{r}) \exp [i\phi(\mathbf{r})], \quad (1)$$

where $\phi(\mathbf{r}) = \pi\lambda \int U(\mathbf{r}, z)\, dz$ is the phase shift calculated as an integral over the Coulomb potential distribution $U(\mathbf{r}, z)$ within the object, λ is the wavelength of the electrons, $\mathbf{r}$ is a vector in the coordinate plane perpendicular to the incoming beam, and z is the coordinate in the direction of the incoming beam. With no loss of generality, we may normalize the amplitude of the incident plane wave to unity at the entrance surface of specimen, $\tau_{in}(\mathbf{r}) = 1$. In the weak-phase approximation, $\phi(\mathbf{r}) \ll 1$, Eq. (1) can be rewritten as

$$\tau_{out}(\mathbf{r}) = 1 + i\phi(\mathbf{r}). \quad (2)$$

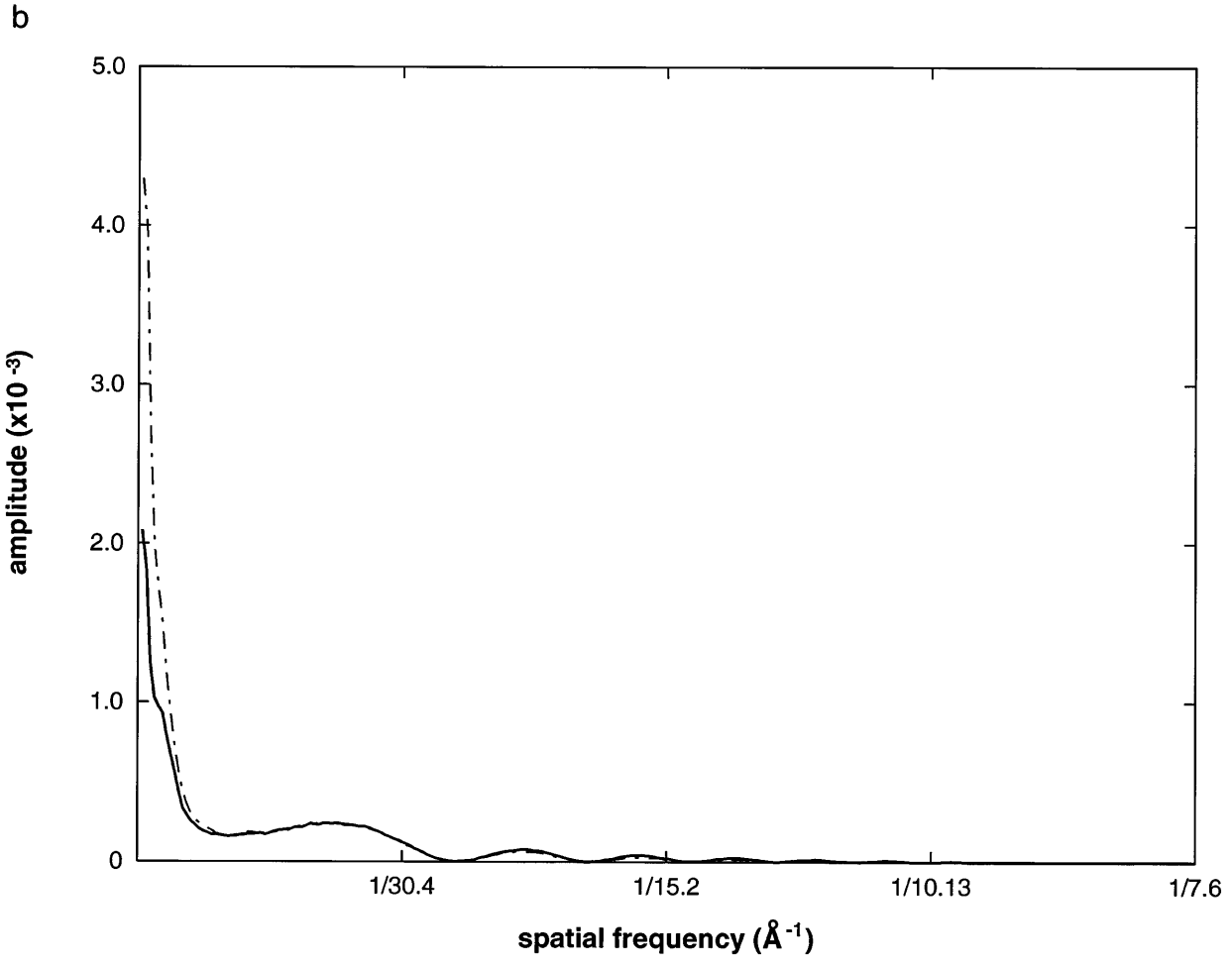

FIG. 2—*Continued*

In the presence of absorption, the object will have both phase and amplitude components, and Eq. (1) will become instead

$$\tau_{out}(\mathbf{r}) = 1 + i\phi(\mathbf{r}) + \mu(\mathbf{r}), \tag{3}$$

where the amplitude component $\mu(\mathbf{r})$ describes a spatial modulation resulting from electrons scattered into large angles and removed by the object aperture and from inelastically scattered electrons removed by the energy filter. We will denote the Fourier transform of the scattered wave in Eq. (3) as $T_{out}(\mathbf{k})$, where $\mathbf{k}$ is a vector in Fourier space related to the scattering angle θ by $\mathbf{k} = \theta/\lambda$. $\Phi(\mathbf{k})$ and $M(\mathbf{k})$ are the Fourier transforms of $\phi(\mathbf{r})$ and $\mu(\mathbf{r})$, respectively. Since the extra phase shift due to lens aberrations and defocus is exp $[i\gamma(\mathbf{k})]$, it follows that

$$T_{out}(\mathbf{k}) = [\delta(\mathbf{k}) + i\Phi(\mathbf{k}) + M(\mathbf{k})] \exp [i\gamma(\mathbf{k})], \tag{4}$$

where, under the assumption that the axial astigmatism is negligible,

$$\gamma(\mathbf{k}) = 2\pi(-0.5\Delta z\lambda\mathbf{k}^2 + 0.25C_s\lambda^3\mathbf{k}^4). \tag{5}$$

Δz is the defocus, C_s the third-order spherical aberration constant. Under this approximation $\gamma(\mathbf{k})$ is rotationally symmetric, denoted henceforth as $\gamma(k)$, with $k = |\mathbf{k}|$.

The image intensity is given by $\tau^*_{out}(\mathbf{r})\tau_{out}(\mathbf{r})$. It follows that the Fourier transform of the image intensity is the convolution product $I(\mathbf{k}) = T_{out}(\mathbf{k}) \otimes T_{out}(-\mathbf{k})$. Since $\Phi(\mathbf{k}) \ll 1$ and $M(\mathbf{k}) \ll 1$, we can neglect the quadratic terms and obtain

$$I(\mathbf{k}) = \delta(\mathbf{k}) + 2[\Phi(\mathbf{k}) \sin \gamma(k) - M(\mathbf{k}) \cos \gamma(k)]. \tag{6}$$

This is the essence of the linear contrast transfer theory summarized by Wade (1992). We can define $M(\mathbf{k}) = W(\mathbf{k})\Phi(\mathbf{k})$, where $W(\mathbf{k})$ is the ratio of amplitude to phase component. For negatively stained images, most amplitude contrast is produced by heavy atoms, while for unstained frozen-hydrated images of biological specimens, the amplitude contrast is similar for all atoms. The term $W(\mathbf{k})$ can be assumed to be constant in the spatial frequency range considered and will be called *amplitude contrast ratio*. Thus, Eq. (6) can be rewritten as

$$I(\mathbf{k}) = \delta(\mathbf{k}) + 2\Phi(\mathbf{k})[\sin \gamma(k) - W \cos \gamma(k)]. \tag{7}$$

Eq. (7) shows that, in the framework of the weak-phase approximation, the electron-optical aberrations do not destroy the linear relationship between the Fourier transforms of the image inten-

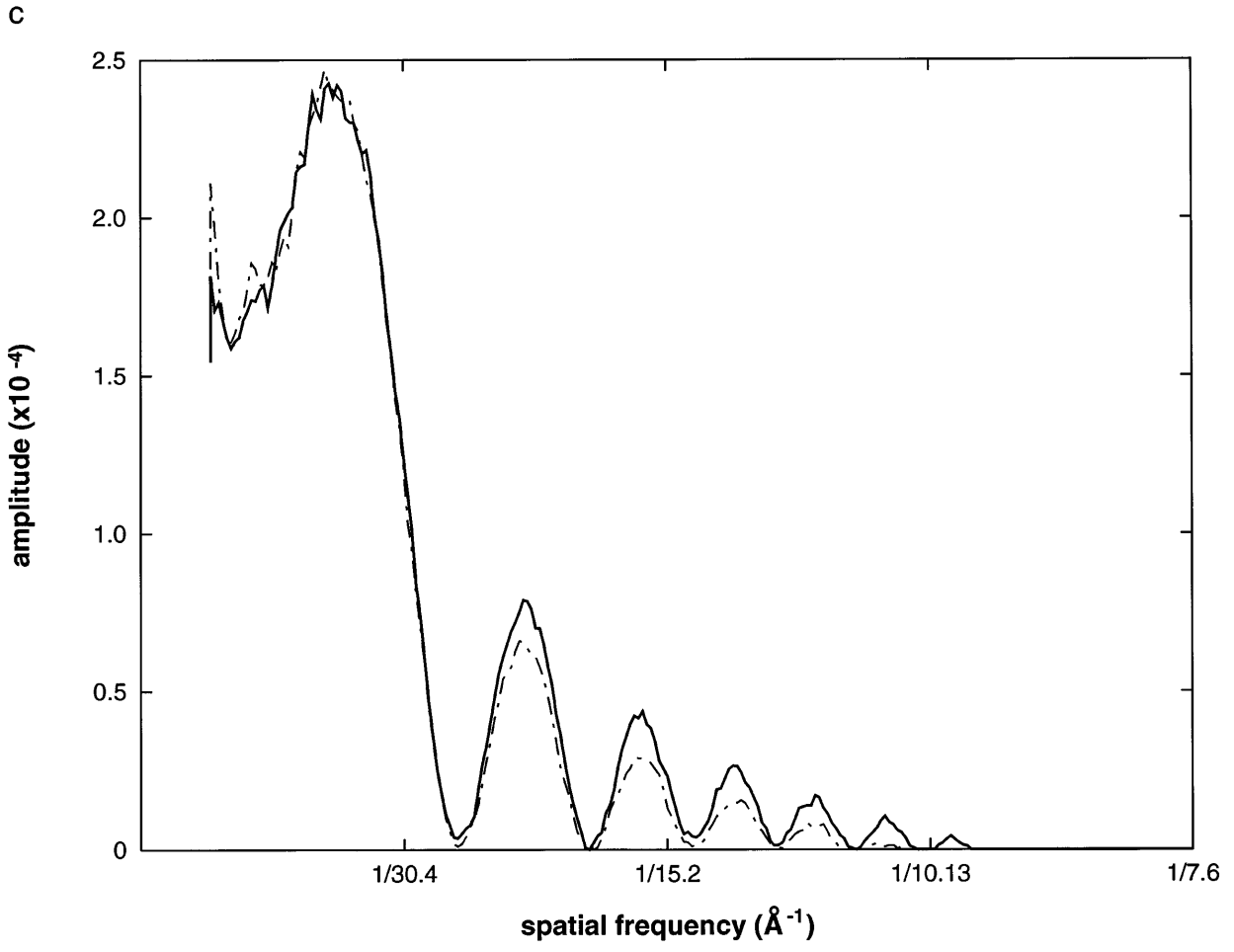

FIG. 2—*Continued*

sity and the projected potential of the object. Thus, the contrast transfer function has the explicit form

$$H(k) = 2[\sin \gamma(k) - W \cos \gamma(k)]. \quad (8)$$

In practice, we never have a perfectly parallel, monochromatic incident electron beam. The partial coherence prevailing under experimental conditions attenuates the CTF at high frequencies. The effects are approximately described by envelope functions (Frank, 1973; Wade and Frank, 1977). The envelope function for finite source size with a Gaussian distribution (Frank, 1973) is described as

$$E_{pc}(k) = \exp [-\pi^2 q^2 (k^3 C_s \lambda^3 - \Delta z k \lambda)^2], \quad (9)$$

where q is the effective source size associated with the illumination system. The envelope function for energy spread (Wade and Frank, 1977) is

$$E_{es}(k) = \exp \left[-\frac{1}{16 \ln 2} \pi^2 \delta z^2 k^4 \lambda^2 \right], \quad (10)$$

where δz is the effective defocus variation associated with the energy spread. Resolution limiting effects associated with the recording are described by the modulation transfer function of the film (Downing and Grano, 1982)

$$E_f(k) = 1/[1 + (k/k_f)^2], \quad (11)$$

where k_f is a characteristic spatial frequency. The Gaussian envelope function (Kenney *et al.*, 1992) which summarily accounts for drift, specimen charging effects, and multiple inelastic–elastic scattering is

$$E_g(k) = \exp [-(k/k_g)^2], \quad (12)$$

where k_g is the halfwidth of the Gaussian function in Fourier space.

Considering additive noise $N(\mathbf{k})$, the final image intensity in Fourier space can be expressed as

$$I(\mathbf{k}) = E_{pc}(k) E_{es}(k) E_f(k) E_g(k) H(k) \Phi(\mathbf{k}) + N(\mathbf{k}). \quad (13)$$

To estimate unknown parameters in Eq. (13) it is convenient to estimate the power spectrum by averaging $|I(\mathbf{k})|^2$ over large parts of the micrographs. In addition, since Eqs. (8)–(12) are rotationally symmetric (it was assumed that the axial astigmatism of the microscope is negligible), the two-dimensional power spectrum estimate can be rotationally averaged. This reduces the error of the estimate and allows the minima of the power spectrum to be

located easily. Thus, assuming that the signal $\Phi(\mathbf{k})$ is not correlated with the noise $N(\mathbf{k})$ and that the power spectrum of signal is approximately constant in the interesting frequency range, the observed rotationally symmetrized power spectrum is given by

$$S^2(k) = [E_{pc}(k)E_{es}(k)E_f(k)E_g(k)H(k)]^2 + S_N^2(k), \tag{14}$$

where $S(k)$ and $S_N(k)$ are the square roots of the radial distributions of the power spectra of the observed image and background noise, respectively. The background noise is due to the random statistical fluctuations of the optical density from several sources: shot noise, or the statistical variation in the number of electrons incident within portions of uniformly exposed areas; fog noise, or noise caused by grains that develop without having been struck by electrons; variations in the number of grains made developable by each electron; and quantum noise of elastic and inelastic scattering. We describe the square root of this complicated, not well-characterized, spatial frequency-dependent noise distribution by a Gaussian profile:

$$S_N(k) = a + b \exp[-(k/c)^2], \tag{15}$$

where a, b, and c are heuristic parameters that have to be determined.

We will use Eq. (14) to describe our experimental results, in which defocus Δz and amplitude contrast ratio W in $H(k)$, q in $E_{pc}(k)$, δz in $E_{es}(k)$, k_f in $E_f(k)$, k_g in $E_g(k)$ and a, b, c in $S_N(k)$ need to be determined.

Determination of some of these parameters has been previously approached. Downing and Grano (1982) studied the emulsion spectrum of the negative and described its profile by an exponential function. The size of the amplitude component has been evaluated by different methods: Erickson and Klug (1971), Toyoshima and Unwin (1988), and Toyoshima *et al.* (1993) compared the amplitudes of crystal reflections at different defocus settings; Typke and Radermacher (1982) used astigmatism to generate a zero-order minimum where the phase term and amplitude term cancel each other out.

An accounting for the effects of the envelope functions is important for recovering the actual weights affecting the Fourier transform at different frequencies. Thus far, only a few groups have considered the envelope functions. Zhou and Chiu (1993) described the envelope functions by a polynomial function; Möbus and Rühle (1993) extracted the parameters of the envelope functions using astigmatism to generate defocus dependence within the same micrograph.

Altogether, we need to evaluate nine parameters in Eq. (14). As follows from the theory, in the absence of the background noise the 1D profile of the power spectrum of the micrograph field should have zeros at locations corresponding to the zeros of the CTF. Due to the presence of the additive background noise (term $S_N^2(k)$) the minima in the observed power spectrum (Fig. 3a) are above zero. This suggests that instead of trying to fit the entire curve given by Eq. (14) directly to the 1D profile of the power spectrum estimate, we can look for the minima of this profile and use their *locations* to find the parameters a, b, c of the background noise $S_N(k)$ along with defocus Δz and amplitude contrast ratio W in $H(k)$. These parameters depend on the positions of the power spectrum minima, not on the general shape of this estimate. In this way the whole process of the CTF parameters retrieval is decomposed into separate steps, which makes this procedure more robust and less sensitive to dependencies among CTF parameters.

In summary the steps in the CTF parameters retrieval procedure proposed are as follows: (1) calculate a 2D estimate of the power spectrum of the micrograph; (2) calculate the 1D rotational average of this estimate; (3) determine the locations of the minima of the 1D rotational average; (4) determine parameters a, b, c in background noise distribution profile $S_N(k)$ from the locations of the minima; (5) determine defocus Δz and amplitude contrast ratio W in $H(k)$ using the locations of the minima; (6) determine q, δz, k_f, k_g and refine the amplitude contrast ratio W using the 1D rotational average corrected for the background noise.

Robust estimation of the power spectrum is an important first step of the CTF retrieval procedure. In our approach we use a method of estimation through *averaged overlapping periodograms*. A similar approach was developed independently by Fernandez and Carazo (1997).

For a finite, discrete time series the periodogram is defined as the squared magnitude of the discrete Fourier transform. However, the periodogram is known to be a biased estimate of the power spectrum (Schuster, 1898). What is even more problematic, the periodogram is not a consistent estimate of the power spectrum; i.e., its variance does not approach zero with increasing window size. In practical terms, this means that the periodogram can be expected to fluctuate rather wildly about the true power spectrum. The method of averaged overlapping periodograms (Welch, 1967) is designed to improve the statistical properties of the estimate.

When K identically distributed independent measurements are averaged, the variance of the average is decreased with respect to the individual variance by the ratio (Welch, 1967)

$$\frac{\delta_{avg}^2}{\delta_{meas}^2} = \frac{1}{K}, \tag{16}$$

where δ_{avg}^2 is the variance of the average and δ_{meas}^2 is the variance of the individual measurement. If we use overlapping areas, the periodograms are no longer independent. In this case the variance ratio becomes (Welch, 1967)

$$\frac{\delta_{avg}^2}{\delta_{meas}^2} = \frac{1}{K}[1 + 2c^2(t)] - \frac{2}{K^2}[c^2(t)], \tag{17}$$

where $c(t)$ is the correlation coefficient between overlapped areas and t is the percentage of overlapping. The correlation coefficient between windows $W(l)$ is given by (Harris, 1978)

$$c(t) = \frac{\sum_{l=0}^{tL-1} [W(l)W(l + (1-t)L)]}{\sum_{l=0}^{L-1} W^2(l)}, \tag{18}$$

where $W(l)$ is the window function, L is the window length. For rectangular window and t equal to 0.5, $c(t)$ is 0.5 (Harris, 1978).

The variance of the estimate decreases as the number of windows that are obtained by dividing the image into small pieces increases. But, since the resolution of the estimate decreases as the size of window decreases, a balance between number of windows chosen and their size has to be found. In our application, we chose a window size of 512×512 pixels and an overlap of 50%. For a typical size of the micrograph field (approximately 3500×3500 pixels), this means that 49 windows are available for averaging. According to Eq. (16), for $K = 49$ and 50% overlap, the variance of the average will be reduced to 0.03 with respect to the average of a single measurement. Further reduction of the variance is achieved by rotational averaging of the 2D power spectrum estimate. The resulting 1D profile is finally used in the third step of our procedure. Its minima are located and used in steps four and five.

As was pointed out before, the parameters a, b, c in Eq. (15) should be such that the Gaussian curve $S_N(k)$ coincides with the minima of the 1D profile of the power spectrum. After these

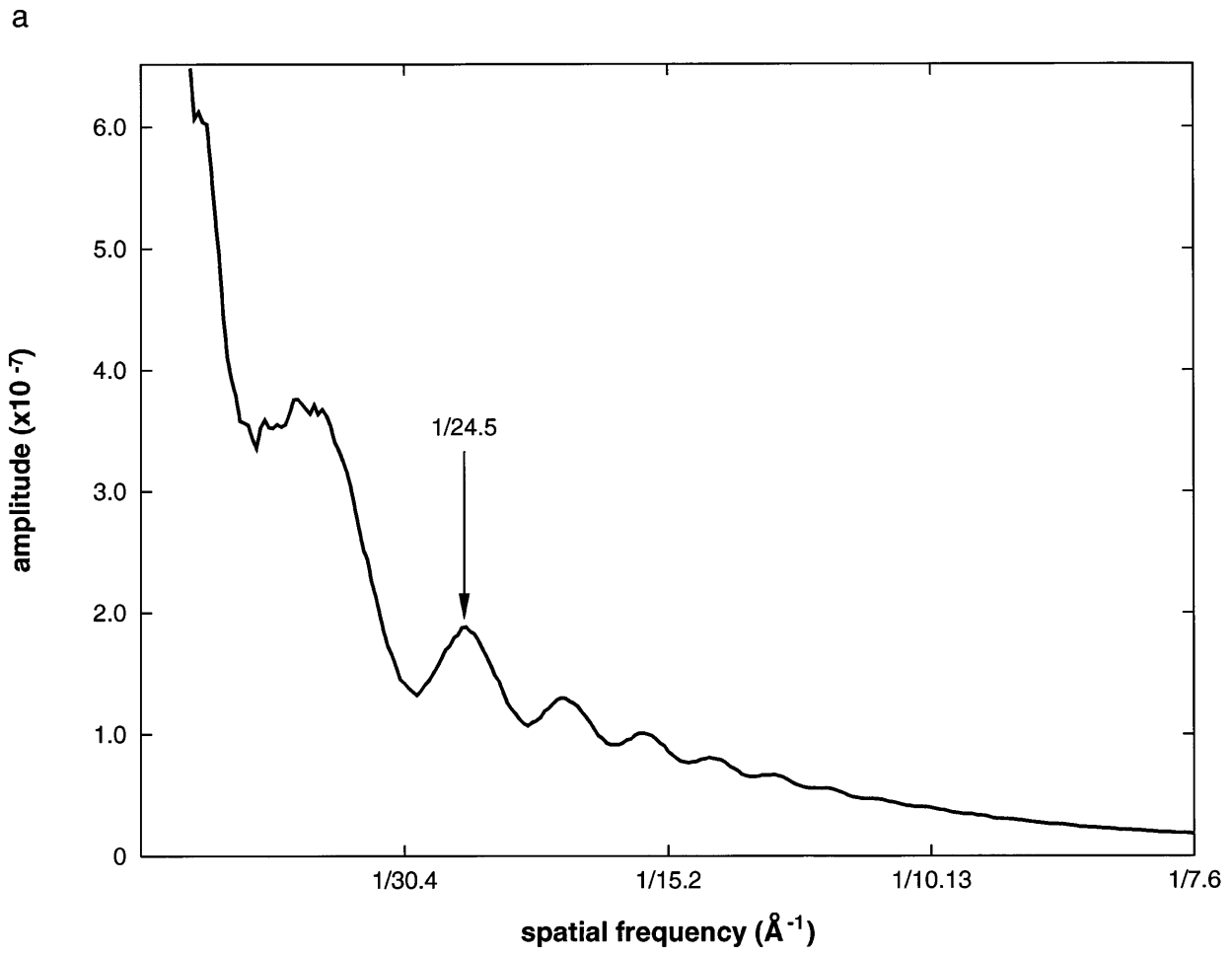

FIG. 3. Estimation of CTF using the rotationally averaged power spectrum. The solid line is the experimental 1D profile, the dashed line is the simulated 1D profile. (a) 1D profile of rotationally averaged power spectrum with the low-spatial-frequency peak masked out; (b) 1D profile of (a) with background noise subtracted, so that all the minima are brought down to 0; (c) background-corrected 1D profile and theoretical profile calculated using Eq. (8) with estimated parameters; (d) background-corrected 1D profile and theoretical profile using Eq. (13) with estimated parameters. The amplitude of 1D profiles is in arbitrary unit.

parameters have been estimated by means of the least-squares fit procedure and the background noise has been subtracted, the resulting curve (Fig. 3b) has a shape more similar to that predicted by theory. To make this approach more robust we can use the additional stipulation that the halfwidth of the Gaussian profile c should be both defocus-independent and source size-independent. Thus, in case there are only a few zeros in the CTF, which could cause large errors in the estimation, we can improve the accuracy by using more than one micrograph with the constraint that c should be the same for all. For the worst case, in which there is only one minimum found in the profile, a is set to zero and c is supplied. The profiles with background noise deleted are later used in the final, sixth step of the CTF parameters estimation procedure (see below).

In the fifth step, the defocus values and the size of the amplitude contrast ratio are determined using the least-squares method to fit the positions of the minima to the zeros of Eq. (8). Various constraints can be added to the fitting process, such as defined, constant defocus steps or same amplitude contrast ratio within the defocus series. Only the same amplitude contrast ratio constraint was used in evaluating a defocus series. An experimental 1D profile and a simulated 1D profile without considering the envelope function are shown in Fig. 3c.

Four parameters determine resolution limiting effects described by the envelope functions (Eqs. (9)–(12)): q in $E_{pc}(k)$, k_g in $E_g(k)$ and k_f in $E_f(k)$. The effective defocus variation δz in $E_{es}(k)$ is associated with the defocus spread, which is caused by high-voltage fluctuations, lens current fluctuations, and defocus variations within the specimen. The first two sources of defocus spread are relatively small compared to the defocus variation within ice thickness, which was estimated to be approximately 500–600 Å, using Berriman's method (J. Berriman, personal communication, 1993). In this method, a hole is burnt in the ice layer at +45° tilt by focusing the electron beam narrowly. Inspection of the specimen at −45° specimen tilt then allows the depth of the hole to be measured. We decided to use the value of 600 Å as the basis for estimating the energy spread envelope function without attempting to determine this function experimentally. Thus, what remained to be determined were three parameters in the sixth step of the procedure using the whole background-corrected profile and the already determined defocus and amplitude contrast ratio values.

The partial coherence envelope function $E_{pc}(k)$ and envelope function $E_g(k)$ due to other combined effects such as charging are very similar in their spatial frequency dependency. However, since $E_{pc}(k)$ is defocus-dependent, as shown in Fig. 4, whereas $E_g(k)$ is not, the use of a defocus series makes it possible to differentiate between $E_{pc}(k)$ and $E_g(k)$ and estimate q and k_g from the

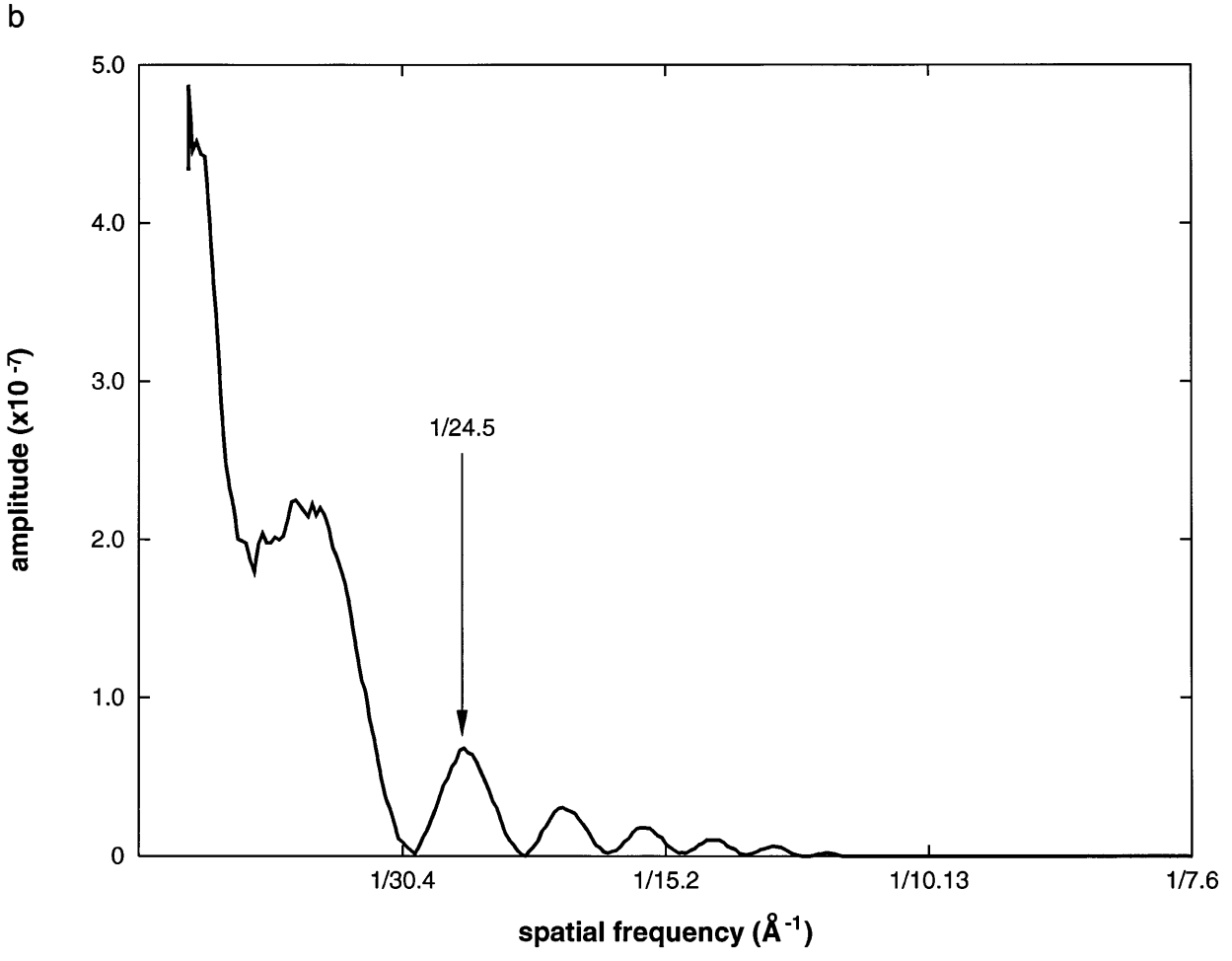

FIG. 3—*Continued*

respective equations. The modulation transfer function of the film $E_f(k)$ decreases much more slowly than either $E_{pc}(k)$ or $E_g(k)$ as the spatial frequency increases; thus, it is easy to differentiate it from these two envelope functions. As the error of estimation of the amplitude contrast ratio W decreases in the low-frequency range, the addition of more low-frequency data points in the least-squares fitting procedure will improve the estimation of W. The experimental and estimated profiles obtained are shown in Fig. 3d.

2.3 3D Reconstruction with CTF Correction

The problem of 3D reconstruction can be treated as an algebraic one. If we describe the projection operation by a non-square matrix P, then the relationship between the 3D structure U and the projections ϕ can be written as

$$\phi = PU. \tag{19}$$

If the total number of data points in N projections exceeds the number of voxels in the 3D structure, which usually is the case in EM applications, Eq. (19) constitutes an overdetermined system of linear equations. A least-squares method can be used to find a solution:

$$|\phi - PU|^2 \rightarrow \min, \tag{20}$$

Because of the presence of noise, the inconsistency among the data and gaps in angular distribution of projections, P has a nontrivial null space in the set theoretical description of this procedure (Carazo, 1992). To obtain a unique solution we employed the linear regularization method (Press *et al.*, 1992) by adding the requirement of smoothness of the solution U in terms of the square Laplacian of U:

$$(1 - \kappa)|\phi - PU|^2 + \kappa|BU|^2 \rightarrow \min, \tag{21}$$

where matrix B is a discrete approximation of the Laplacian and κ is a Lagrange multiplier. The value of κ determines the relative smoothness of the solution U. The projection ϕ modified by the CTF yields the images i measured by the electron microscope, where i is the reverse Fourier transform of $I(\mathbf{k})$ in Eq. (13). The resulting CTF-modified projections are denoted by d. In real space, the effect of the CTF can be described by a point spread function, represented by a square matrix $\hat{C}$. Therefore, Eq. (21) has to be rewritten as

$$(1 - \kappa)|d - P\hat{C}g|^2 + \kappa|Bg|^2 \rightarrow \min, \tag{22}$$

where g is the CTF-corrected 3D structure. Theoretically, the CTF is a 2D function and is only defined for projections. However, because $\hat{C}$ is rotationally symmetric in Fourier space we can apply its 3D version directly to the 3D distribution g. The solution of Eq.

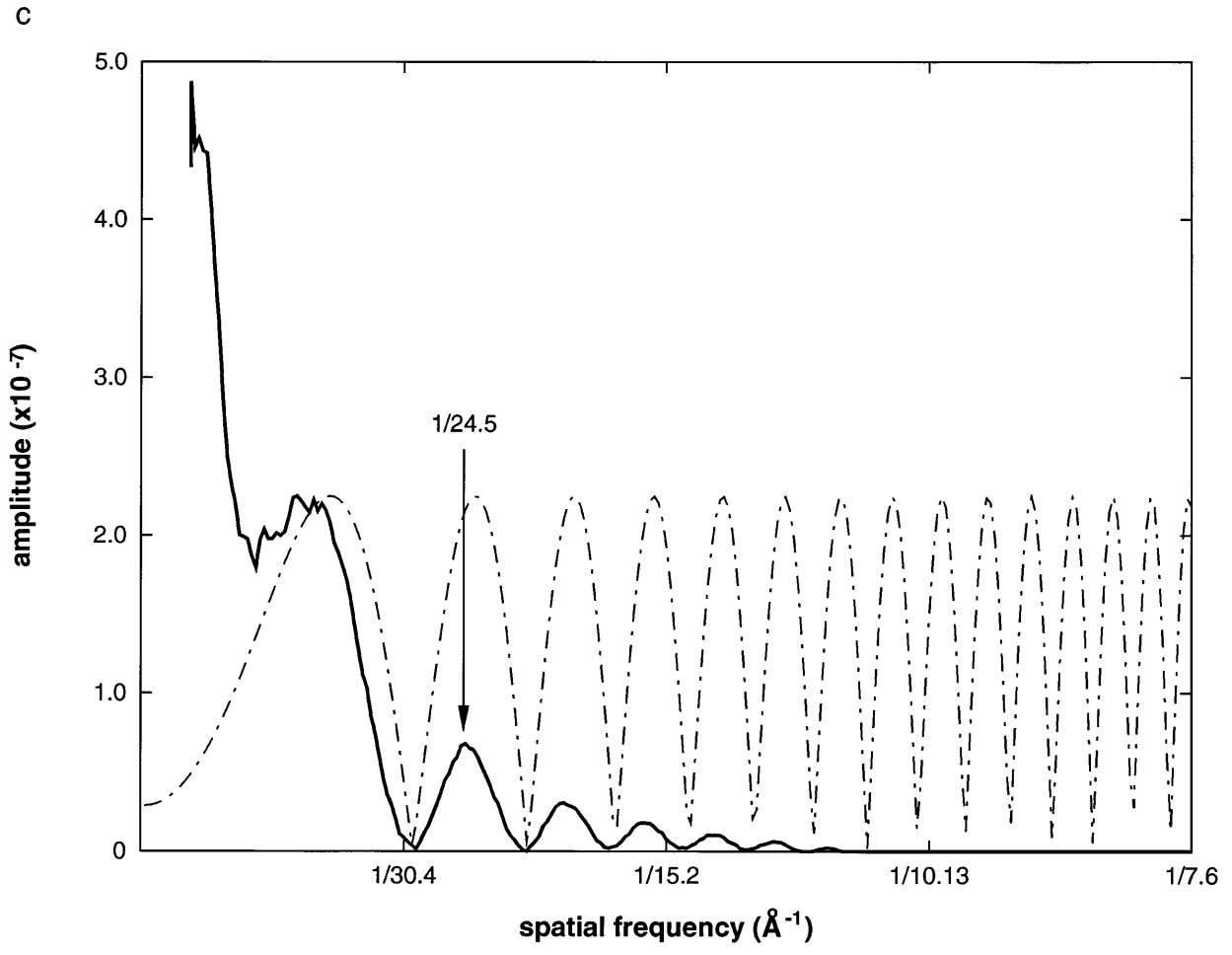

FIG. 3—*Continued*

(22) can be found using the steepest-descent method, in which an initial guess $g^{(0)}$ for a solution is iteratively modified in the direction of the local gradient:

$$g^{(n+1)} = g^{(n)} + \rho[(1-\kappa)\hat{C}^T P^T[d - P\hat{C}g^{(n)}] - \kappa B^T B g^{(n)}], \quad (23)$$

where $\rho > 0$ is a relaxation constant controlling the convergence speed and $\hat{C}^T$, P^T, and B^T are the transposes of $\hat{C}$, P, and B, respectively. To combine data sets obtained with different defocus settings, Eqs. (22) and (23) have to be modified in the following way:

$$\sum_{i=1}^{m} (1-\kappa)|d_i - P_i\hat{C}_i g|^2 + \kappa|Bg|^2 \rightarrow \min, \quad (24)$$

$$g^{(n+1)} = g^{(n)} + \rho\left[(1-\kappa)\sum_{i=1}^{m} \hat{C}_i^T P_i^T[d_i - P_i\hat{C}_i g^{(n)}] - \kappa B^T B g^{(n)}\right], \quad (25)$$

where m is the number of data sets. In the EM application, the number of projections usually exceeds the linear size of the volume by at least an order of magnitude. It is therefore convenient to rewrite Eq. (25) to avoid multiple access to the data d_i:

$$g^{(n+1)} = g^{(n)} + \rho\left[(1-\kappa)\left[\sum_{i=1}^{m} (\hat{C}_i^T P_i^T d_i) - \sum_{i=1}^{k} (\hat{C}_i^T P_i^T P_i \hat{C}_i g^{(n)})\right] - \kappa \mathrm{B^T B g}^{(n)}\right], \quad (26)$$

The first sum can be precalculated and stored as a 3D volume in the computer memory. Thus, the input projections have to be read only once and are never again accessed during the course of the iterations. In addition, the product B^TB is the Laplacian of the 3D volume $g^{(n)}$, which can be calculated more efficiently without actually creating the matrix B^TB. The point spread function is space-invariant, so $\hat{C}_i$ has a block-Toeplitz structure (Biemond *et al.*, 1990), and $\hat{C}_i$ is equal to $\hat{C}_i^T$. $\hat{C}_i$ is a huge matrix; thus, we use the CTF C_i in Fourier space to modify the Fourier transform of the volume instead. The densities g of the 3D volume calculated using this new method of CTF correction are linearly related to the image intensities representing the original mass distribution. Thus, it becomes possible to relate known properties of the biological material to the results of the EM analysis.

The operations of computing Fourier transform, inverse Fourier transform, projection, and back-projection can take advantage of parallel computer architecture. On a four-processor SGI (Silicon

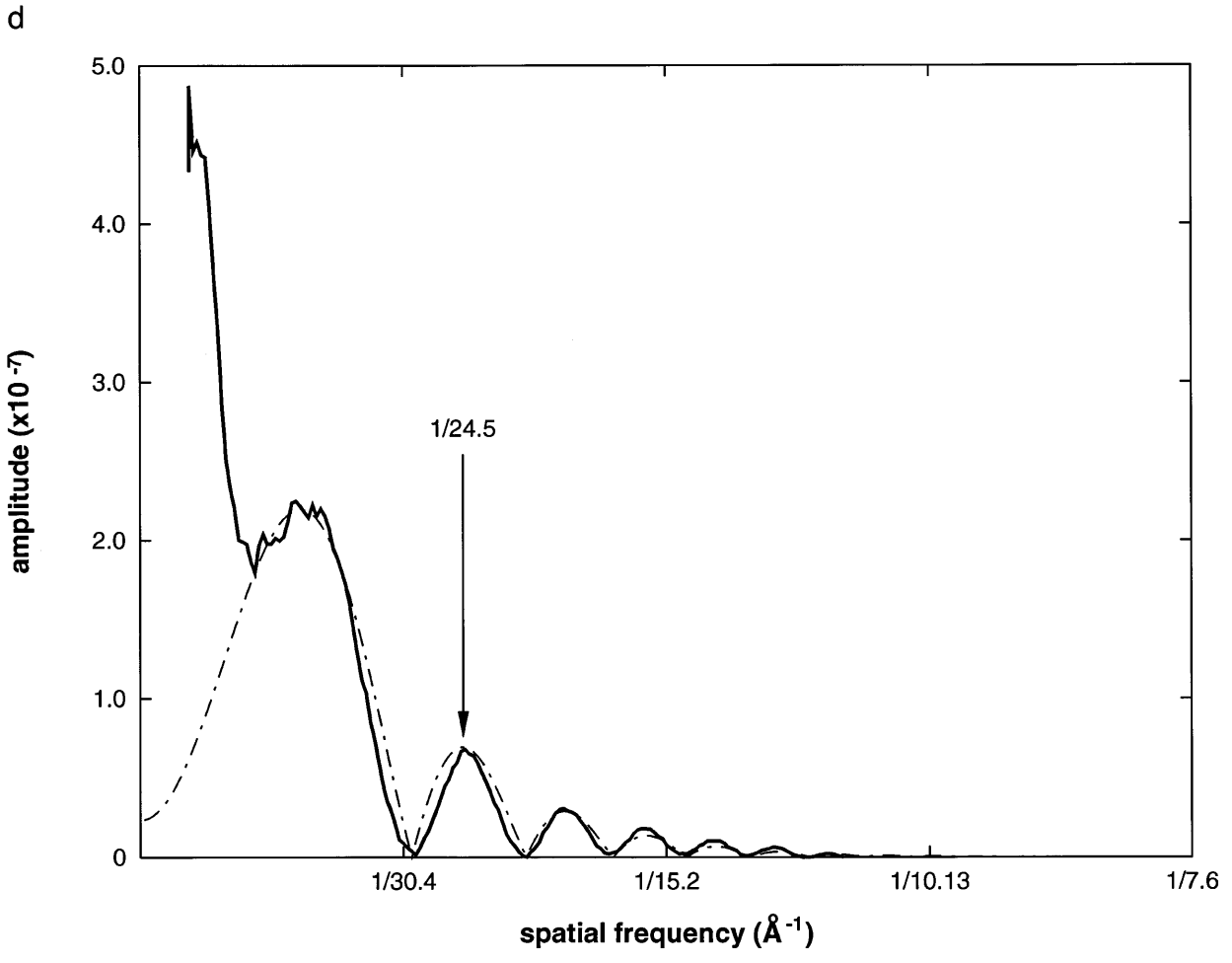

FIG. 3—*Continued*

Graphics, Mountain View, CA) Onyx R8000, the time required for 1 iteration is about 5 min for a volume of 90 × 90 × 90 voxels and 5800 projections. A total of 30 to 50 iterations are typically required to achieve convergence.

3. APPLICATION AND RESULTS

3.1. Data Collection

The specimen was prepared following the procedure of Wagenknecht *et al.* (1988). Molybdenum 400-mesh grids were used to minimize thermal effects. The specimens were examined in a LEO (formerly Zeiss; Oberkochen, Germany) EM912 transmission electron microscope operated at 120 kV. The microscope is equipped with a Köhler illumination system and an Omega energy filter. All the microscopy was done at a temperature below −170°C using a Oxford cryo-holder CT3500 and temperature regulator. A 90-μm objective aperture was used in all experiments. Three images were taken at 0° tilt of the same specimen area using the defocus settings 1.5, 2.0, and 2.5 μm at a magnification of ×52 000, which was calibrated using catalase crystals. With those defocus values and an amplitude contrast ratio of 0.14, the first zeros of CTF are at 1/22.6, 1/26.0, and 1/29.1 $Å^{-1}$, respectively. The dose for each exposure was $5e^{-}/Å^2$; thus, the total dose accumulation reached $15e^{-}/Å^2$ for the data collected at 2.5 μm defocus. The width of the zero-loss energy filter was 14 eV. Images were recorded on Kodak SO163 films and processed in the developer D19 at full strength for 12 min. The negatives were scanned using the Perkin–Elmer flatbed PDS 1010A microdensitometer with a step size of 20 μm. The corresponding pixel size on the specimen is 3.8 Å.

3.2. Image Processing

For all stages of data processing, the SPIDER image processing system (Frank *et al.*, 1981a, 1995c) was used. The CTFs were estimated as described under Methods, Section 2.2; however, we found it necessary to correct each patch of the micrograph for a density ramp effect (Boisset *et al.*, 1993) before calculating the periodogram. Defocus value, ampli-

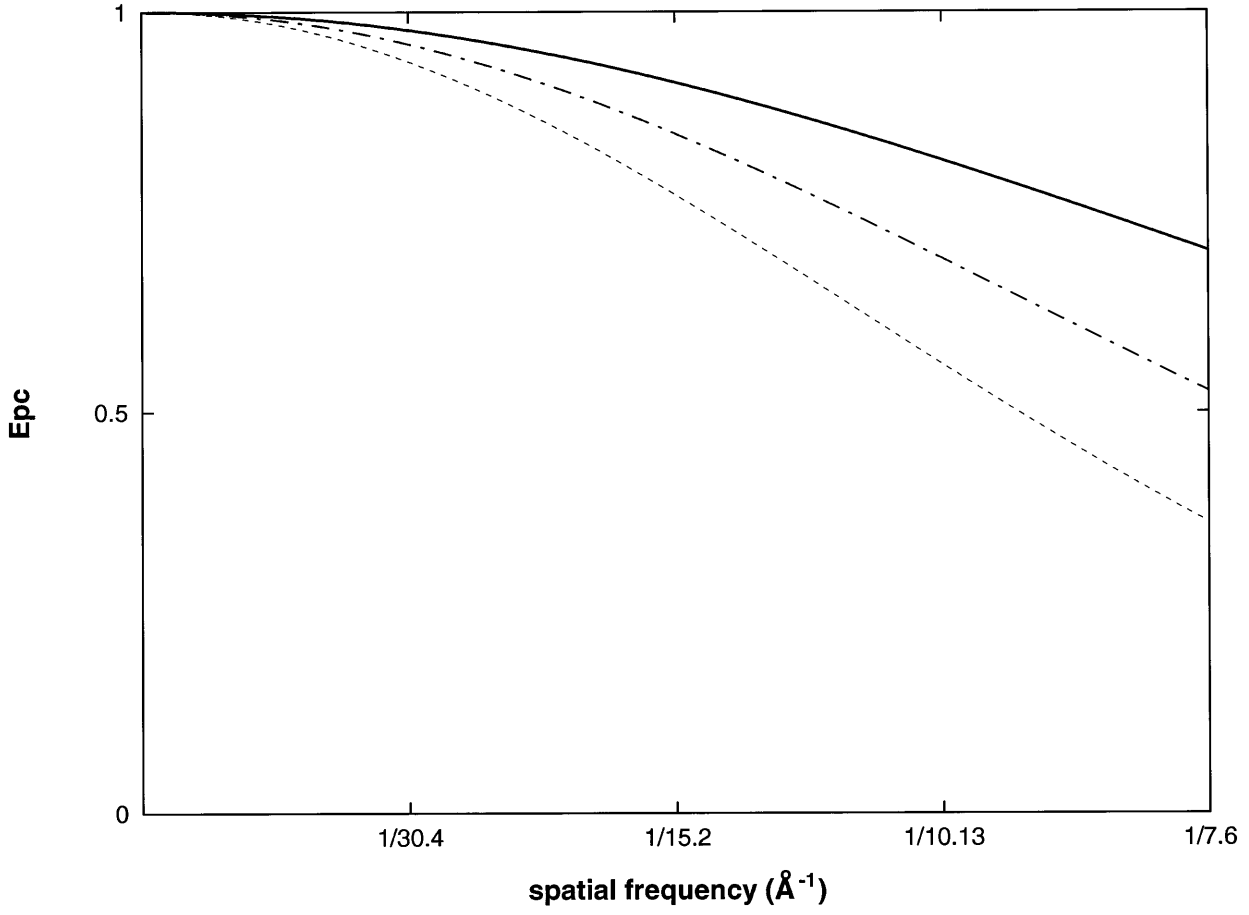

FIG. 4. Defocus dependency of partially coherent envelope function. The wavelength λ is 0.0335 Å, spherical aberration C_s 2.7 mm, and source size 0.003 $Å^{-1}$. Solid line: defocus 1.5 μm; dashed line: defocus 2.0 μm; dotted line: defocus 2.5 μm.

tude contrast ratio, and parameters for the envelope function were determined by least-squares fitting. The amplitude contrast ratio was determined as 0.14. A defocus series and the corresponding power spectra are shown in Fig. 5.

To speed up the windowing of particles we took advantage of the fact that in the defocus series the same field was exposed three times. Thus, initially the particles were selected from the micrograph with the highest defocus. Following a correlation alignment procedure the particles from micrographs with lower defocus were picked automatically. In this procedure (Kessel *et al.*, 1980; for details see Typke *et al.*, 1992), the micrographs are divided into patches, for which the individual shifts are calculated. The shift, rotation, and magnification change for the whole micrograph are subsequently calculated from the shifts of all the patches. The resulting coordinate transformation is applied to the micrograph with lower defocus value, and then the whole procedure is iterated. The accuracy of alignment achieved for the whole image was approximately 0.5 pixel (~2 Å). The final result shows high consistency within the whole micrograph. This means that there are few changes of condition from one exposure to the other and that the local specimen changes due to drift, local warping, and charging are very small. At this point, the accuracy of alignment is limited by the noise in the micrographs (e.g., specks on the negatives and the scanner), the grain size of the emulsion, and the accuracy with which the peak position can be determined.

The particles in each defocus group were then submitted to reference-free alignment (Penczek *et al.*, 1992) and hierarchical ascendant classification using Ward's merging criterion (see Frank, 1990). The resulting cluster averages are shown in Fig. 6. Eulerian angles for aligned images were found using the projection matching method (Penczek *et al.*, 1994) with a θ-angle increment of 2°. A 1/30 $Å^{-1}$ (DPR) reconstruction of the 70S ribosome (Penczek *et al.*, 1994) was used as initial reference. There were 1539, 2043, and 2254 projections available for reconstruction in the 1.5-, 2.0-, and 2.5-μm groups, respec-

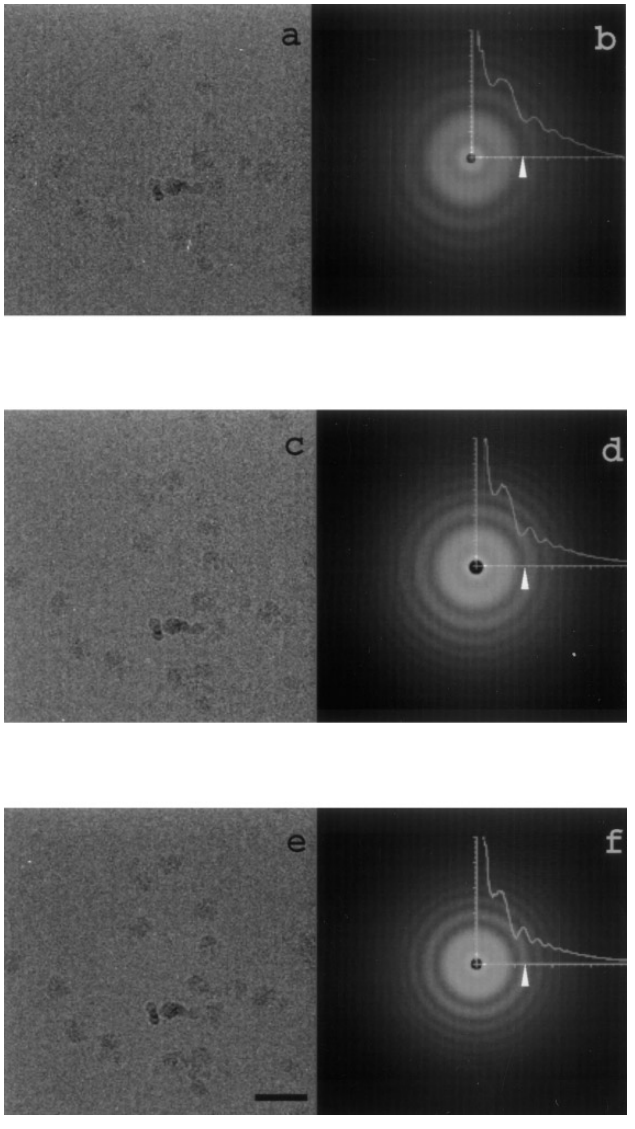

FIG. 5. A defocus series and their power spectra. (a) A 1.5-μm-defocus image field; (b) the corresponding power spectrum. (Insert) Rotational average of the power spectrum with central peak masked out; (c) a 2.0-μm-defocus image of the same specimen area; (d) corresponding power spectrum of (c); (e) a 2.5-μm-defocus image of the same specimen area; (f) corresponding power spectrum of (e). The length of the scale bar is 500 Å.

tively, after exclusion of particles with cross-correlation coefficients smaller than 0.25. This threshold was found to be required to exclude badly aligned projections. The resulting angular distribution is shown in Fig. 7. Reconstructions for each group were calculated following the algorithm given by Eq. (21). The volumes are shown in Fig. 8 and the corresponding resolutions are listed in Table 1. The merged reconstruction from all three groups, calculated using Eq. (26), is shown in Fig. 9.

To use Eq. (26) we have to choose parameters κ (related to the spatial frequency limit), ρ (relaxation parameter), and number of iterations. We choose κ equal to 0.9 so that the spatial frequency limit is 1/14.4 $Å^{-1}$. The combination of number of iteration and ρ value will determine the error in the reconstruction. The error in the reconstructions obtained using Eq. (26) can be separated into two terms. The first term represents the degree of blurring in the reconstruction, and it decreases with increasing iteration number. The second term represents the noise magnification, which increases with the iteration number. The iterative restoration approach as Eq. (26) will have the same noise behavior as the direct restoration approach (e.g., Wiener filtering) when the iteration number goes to infinity (Biemond *et al.*, 1990). This means that in the initial stages of the restoration process the first error quickly diminishes, while in the later stages the amplification of noise begins to dominate the object.

Considering computational time, we always use 50 iterations and vary the ρ value to control the restoration process. The DPR curves for reconstructions from two (2.0 and 2.5 μm) and three (1.5, 2.0, and 2.5 μm) data sets with different ρ values are shown in Figs. 10a and 10b, respectively. For the reconstruction from the two data sets (Frank *et al.*, 1995b) the DPR curve (Fig. 10a) has a surge in the region where the CTF for the 2.5-μm data set reaches 0, which means that a large amount of noise is injected into this region. For three data sets (Fig. 10b), that surge is reduced and has migrated to higher spatial frequencies as a result of the increased amount of signal in the higher frequency range. Thus, the best result of this approach is obtained by using a specific finite number of iterations and ρ value. Unfortunately, the optimal number of iterations and ρ value are usually not known in advance. In the absence of an explicit criterion to judge what is the best combination, there is no better method than by substantially varying both parameters and picking the combination giving the best resolution.

3.3. Refinement

The merged reconstruction was calculated using the CTF correction program Eq. (26), which requires exact values of the CTF parameters for each data set. These values, in particular the defocus value, were estimated using the least-squares method, as discussed under Methods, Section 2.2. To verify that these defocus values result in the optimal resolution of the merged reconstruction, we performed an exhaustive search, varying them around initial values by ± 0.5 μm using a step size of 0.1 μm. For each set of defocus values, the three noncorrected volumes were combined using the Wiener filter approach

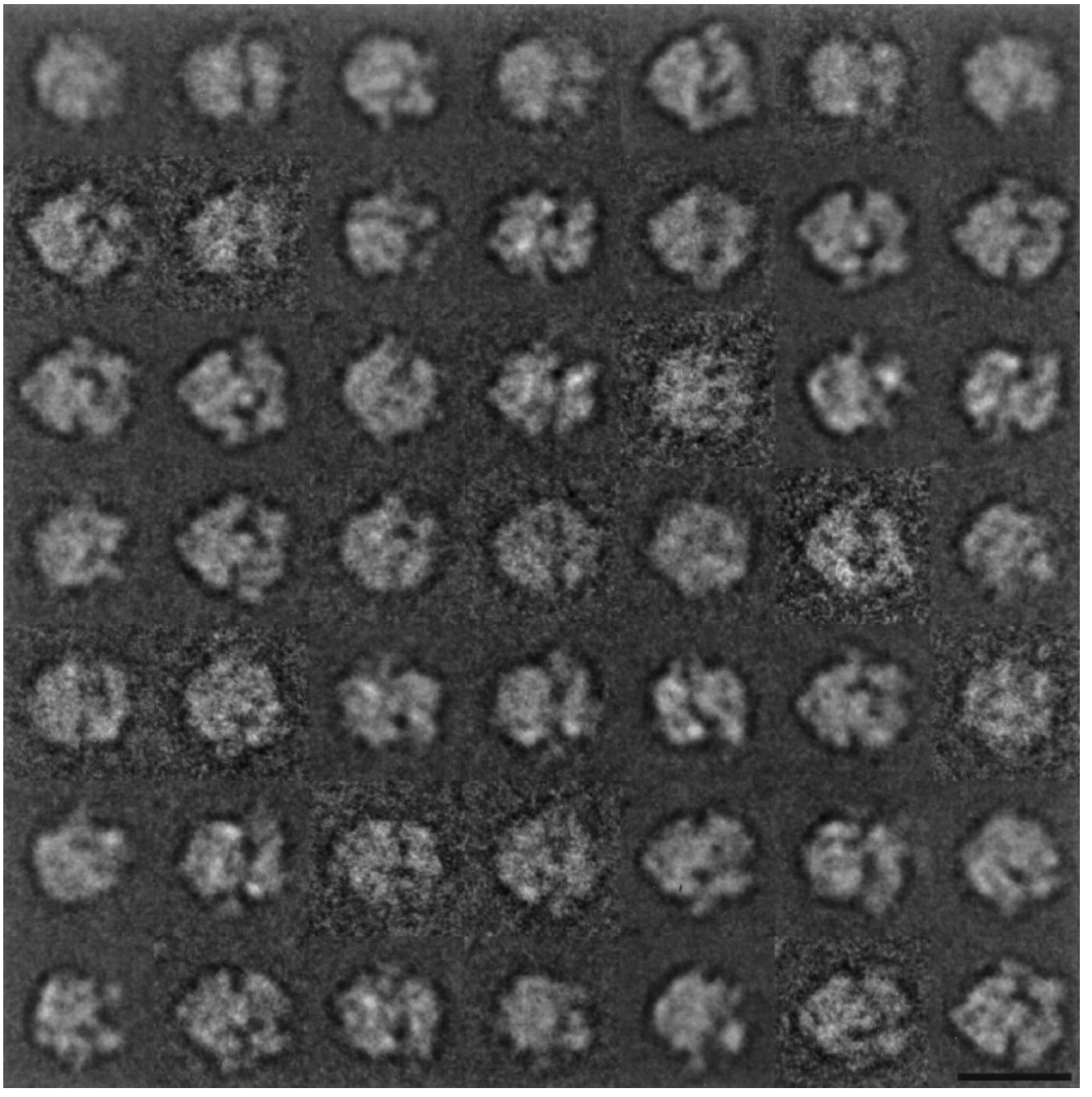

FIG. 6. Averages of 49 classes from 2.5- and 2.0-μm-defocus data sets, determined by hierarchical ascendant classification (see Frank, 1990). The length of the scale bar is 250 Å.

(Schiske, 1973; Frank and Penczek, 1995) and the corresponding resolution was estimated using the DPR criterion. We found that the defocus values of 1.8, 2.1, and 2.6 μm (instead of the initial estimates of 1.5, 2.0, and 2.5 μm) gave the best resolution. This discrepancy between defocus values can be explained by a systematic error in CTF estimation: the thickness of ice in which specimen was embedded was around 0.1 μm, so the defocus value of the specimen would be expected to vary by about that same amount.

Another attempt to improve the resolution was made by assigning an independent CTF for each micrograph. Each data set, 1.5, 2.0, or 2.5 μm, comprises about 10 micrographs, and for each micrograph we estimated the parameters of the CTF. The

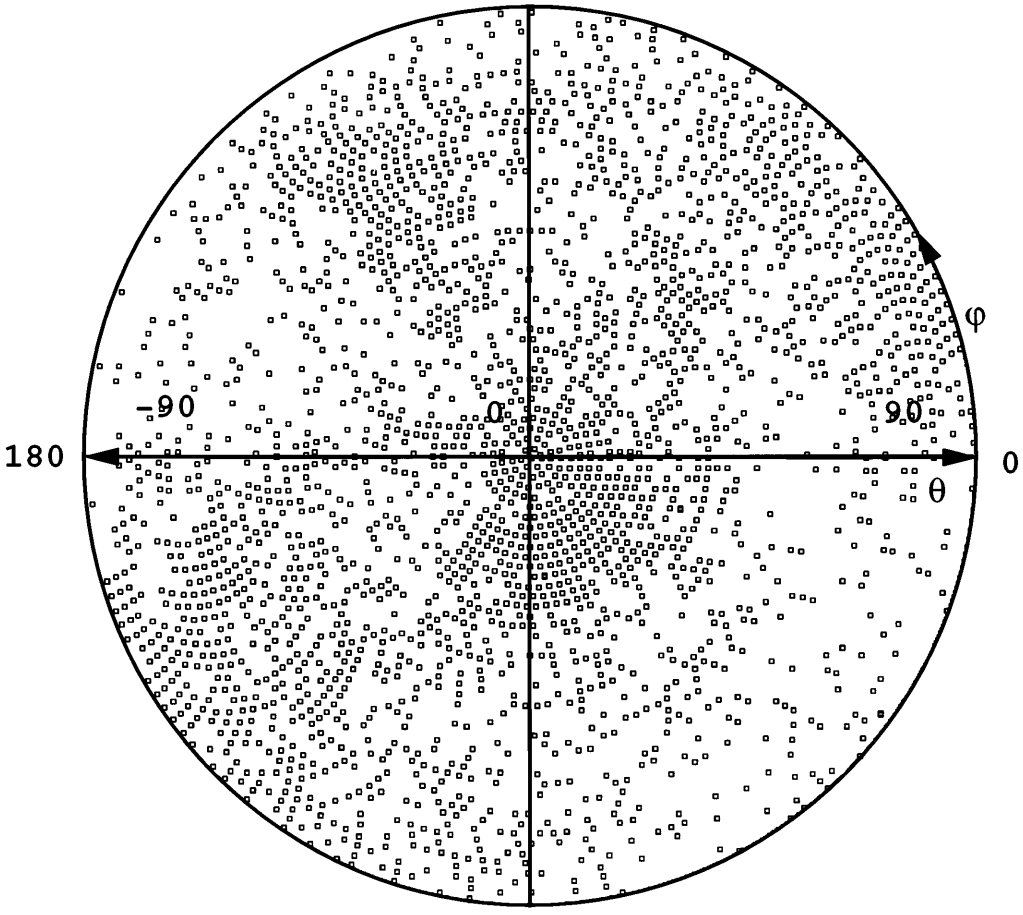

FIG. 7. Eulerian angle distribution of projection directions from all three data sets. Each particle is represented by a point in a (θ, φ) polar coordinate system. The distribution shows that the projections cover almost all the projection angles.

defocus values were found to vary in the range of ±0.25 μm around the average value. However, the use of these more precise defocus values did not result in resolution improvement. The probable cause is that for the volume size used (90 × 90 × 90 voxels) and the estimated defocus variations, the positions of the first zeros of the CTFs are all within the same Fourier pixel. It should be also noted that a certain amount of defocus variations cannot be totally avoided; even if we can correct the systematic error and assign different CTFs to different micrographs, the variations of ice thickness from place to place across the same micrograph will change the defocus values for different particles.

3.4. Histogram of Ribosome Density and Volume Size of Ribosome

The scattering probability derived from energy-filtered cryo-EM data after CTF correction agrees quantitatively with the theoretical prediction (Langmore and Smith, 1992). Thus, the energy filtration allows the mass distribution of biological molecules to be accurately determined. To decide on the appropriate density thresholds for the particle boundary and interior surfaces, we made use of a histogram of densities in the reconstructed volume (Frank *et al.*, 1991; Penczek *et al.*, 1992). The histograms of non-CTF-corrected and CTF-corrected volumes are shown in Fig. 11. Both histograms have a low-density peak, due to the relatively uniform background density of ice, followed by a broader range of medium and higher densities that has to be attributed to protein and RNA. After CTF correction, the ice peak sharpens and a broad peak emerges at the flank of the density range attributed to protein/RNA. The total volume according to the chemical molecular weight is 2.4×10^6 Å^3 and the protein/RNA ratio is 0.72:1.0, considering only protein and RNA (cf. Frank *et al.*, 1991, where an incorrect ratio was used). This volume was estimated using the molecular mass data from Wittmann (1982) and the densities of protein and RNA in ice as given by Langmore and

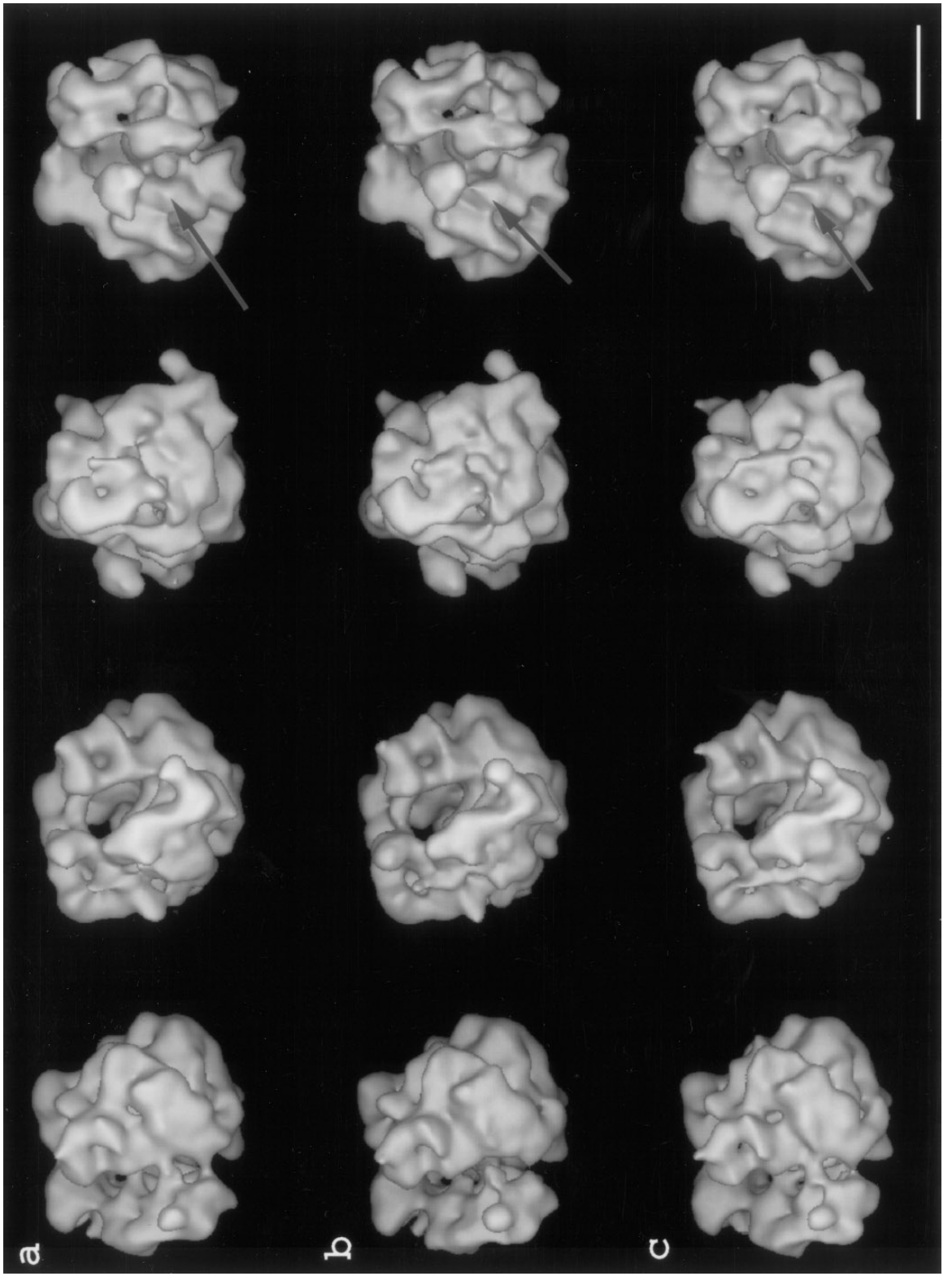

FIG. 8. Comparison of three reconstructions of 70S ribosomes from single-defocus data sets without CTF correction. (a) The reconstruction from the 2.5-μm data set; (b) the reconstruction from the 2.0-μm data set; (c) the reconstruction from the 1.5-μm data set. All the structures are filtered to 1/20 $Å^{-1}$ by a Fermi low-pass filter with temperature equal to 0.03. The same filter is used thereafter for all low-pass filtrations to avoid artifacts introduced into comparisons. The structures are shown from four viewing directions related by 60° rotation around a vertical axis. The structures show minor differences. As the resolution increases, the connection rod (see arrows) for the L1 protein clearly emerges. Scale bar corresponds to 100 Å.

TABLE I

Numbers of Projections Used for 3D Reconstructions and Corresponding Resolutions, as Measured by the Differential Phase Residual Criterion (Frank *et al.*, 1981b)

	First zero in CTF ($Å^{-1}$)	Number of projections	DPR ($Å^{-1}$)
1.5 μm	1/22.6	1539	1/31.1
2.0 μm	1/26.0	2043	1/32.5
2.5 μm	1/29.1	2254	1/34.5
Three sets without CTF correction		5836	1/31.1
Three sets with CTF correction		5836	1/24.5

Smith (1992). The surface representation of the merged reconstruction from three data sets at the density corresponding to a volume size of 2.4×10^6 $Å^3$ is shown in Fig. 9b. The surface of the ribosome is seen to be very fragmented (see Stark *et al.*, 1995, where this choice of volume was used). However, the calculation of chemical molecular weight does not include the presence of salt ions, e.g., Mg^{2+} and K^+, and of spermidine in the ribosome. The ribosome volume estimates from air-dried EM are between 3.00 and 3.56×10^6 $Å^3$; the estimate from freeze-dried EM is even as high as 5.1×10^6 $Å^3$ (van Holde and Hill, 1974). Considering all these factors, we assume a volume increase by 40% from the value derived from the chemical mass, to a total of 3.4×10^6 $Å^3$. Therefore, the density threshold giving a volume of 3.4×10^6 $Å^3$ was used for all surface representations except the one presented in Fig. 9b.

In an attempt to ascertain the effect of resolution limitation on the density distribution, we built a ribosome density model using three components, ice, protein, and RNA, whose densities are given by Langmore and Smith (1992) and whose volume followed the protein/RNA ratio 0.72:1.0, as estimated above. The final reconstruction from the three data sets (1.5, 2.0, and 2.5 μm) was thresholded to obtain the estimated contour of the density corresponding only to RNA. By filling this contour with a single value, a binary representation of the RNA distribution within the ribosome was obtained. A binary representation of the entire ribosome was generated in a similar way. By subtracting the RNA volume from the ribosome volume, we obtained the binary representation of protein alone. The volume not encumbered by protein or RNA was assigned a single density for ice. The three binary models were modified by using three Gaussian random functions with means equal to the densities of ice, protein, and RNA. The density distributions were chosen to be Gaussian to reflect density variations due to packing (protein and RNA) and thickness variation (ice). The final model was built by adding the three resulting density distributions. The model was then low-pass filtered to 1/20 $Å^{-1}$, using the same filter that was applied to all the volumes shown in Figs. 8 and 9.

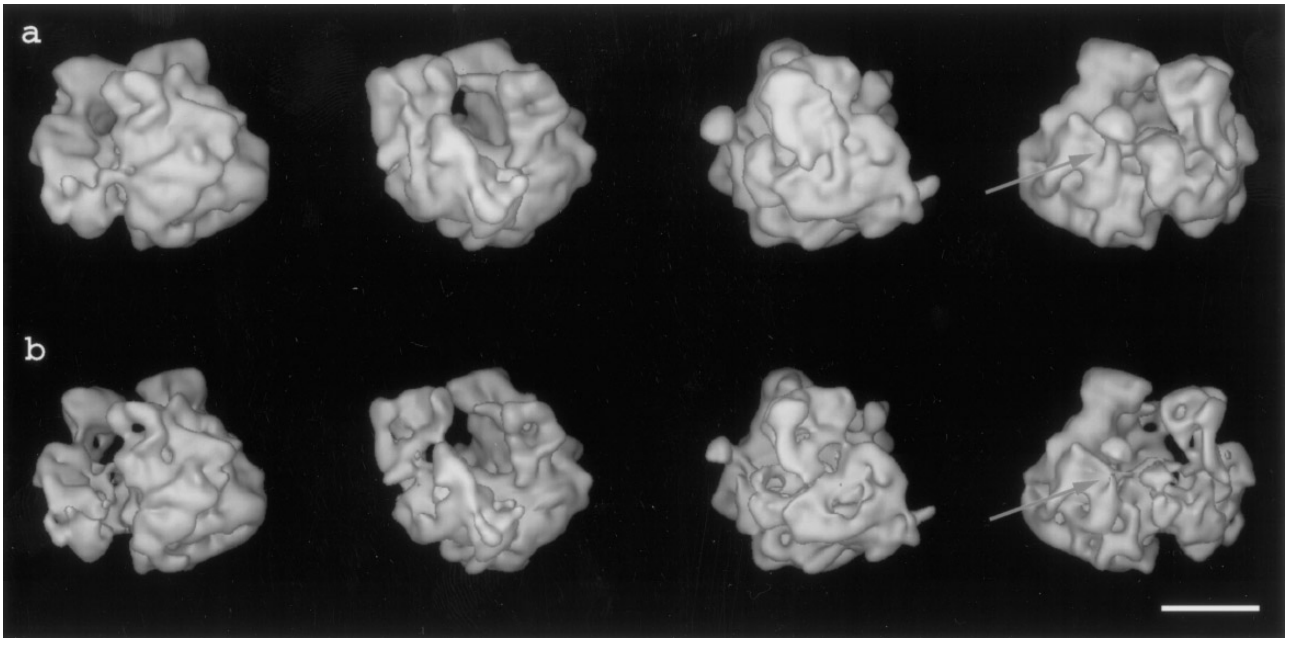

FIG. 9. Surface representation of merged reconstruction from three data sets. (a) The density threshold chosen for the representation corresponds to a volume size of 3.4×10^6 $Å^3$. (b) The density threshold corresponds to the chemical mass, encompassing a volume size of 2.4×10^6 $Å^3$. The arrows point to the L1 connection. Scale bar corresponds to 100 Å.

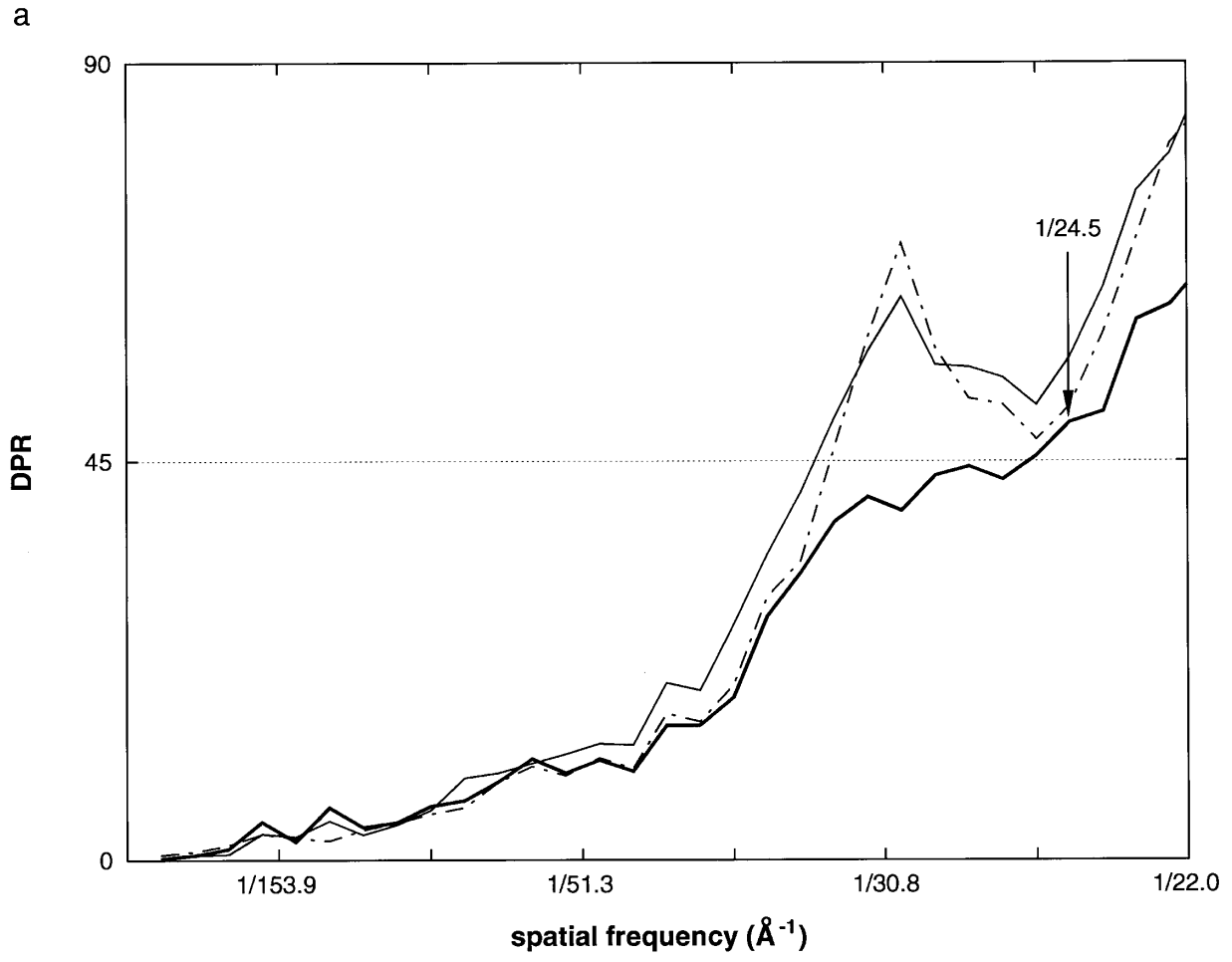

FIG. 10. Comparison of results from Eq. (26) with various combinations of parameters and the result from Wiener filtering. The resolution is measured by differential phase residual (DPR) (Frank *et al.*, 1981b). With carefully chosen ρ, the iterative CTF correction approach (Eq. (26)) performs better than Wiener filtering. Thick solid line: result from Eq. (26) with ρ equal to 1×10^{-5}; thin solid line: result from Eq. (26) with ρ equal to 1×10^{-4}; dashed line: result from Wiener filtering. (a) DPR curves for two data sets (2.0 and 2.5 μm) combined; (b) DPR curves for three data sets (1.5, 2.0, and 2.5 μm) combined.

The histograms before and after low-pass filtration of the model are shown in Fig. 12. After low-pass filtration, the density peak corresponding to protein is seen to disappear, and instead a broad intermediate density range appears between the two remaining peaks. Thus, the appearance of the histogram of the CTF-corrected experimental density (Fig. 11) can be qualitatively explained on the basis of the three-component model. By inference, the broad peak on the right flank of the experimental histogram would be attributed to RNA.

3.5. Validation of Results

The question could be raised to what extent the reference used for angle assignment might determine the outcome. In this work we used a previous 1/30 Å^{-1} reconstruction (Penczek *et al.*, 1994) as our initial reference. The dependency on the reference was tested as follows: the final Eulerian angles determined from projection matching were wobbled by ±15° at random, a low-resolution (1/45.0 Å^{-1}) reconstructed volume was calculated using those angles, and this volume was used as a new initial reference in the projection matching and refinement. The resulting volume is visually identical to volumes described above and agrees with them above the resolution of 1/24.5 Å^{-1}, as determined by the DPR criterion. Thus, the projection matching method proves to be insensitive to the choice of initial reference, and the solution appears to be stable in the resolution range of practical importance in this study. This test is not totally independent, however, since the constructed 1/45.0 Å^{-1} reference still shares low-resolution information with the 1/30 Å^{-1} vol-

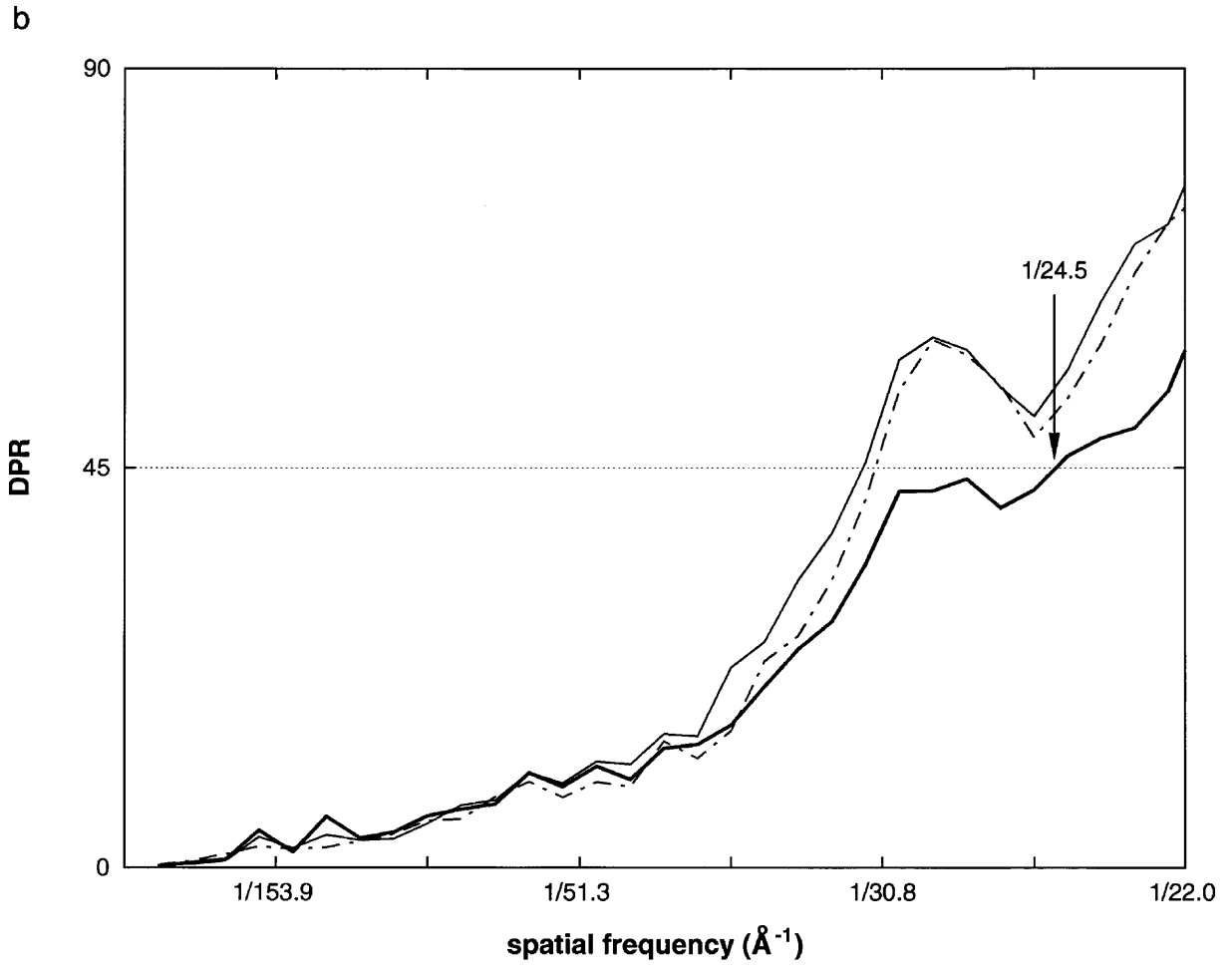

FIG. 10—*Continued*

ume. A truly independent confirmation of the new 70S *E. coli* reconstruction was achieved by determining the orientation of the cluster averages using a common-lines method (Penczek *et al.*, 1996) and then using the resulting volume as initial reference.

DISCUSSION

To obtain an accurate representation of a macromolecular assembly, one must augment the reconstruction from EM images by contrast transfer function correction. In this work we have demonstrated that reconstruction and CTF correction can be combined in a single step. This procedure is not only economical but it can be expected to reduce the accumulation of errors incurred in multistep procedures. That the procedure works is evident from the final 3D map of the ribosome which is characterized by features with high definition, absence of Fresnel fringes at the particle border (as evident from images of cross sections, not shown), and a broadening of the density histogram as expected for a high-pass-filtered two-component object whose original low-spatial-frequency components have been restored.

Having shown the importance of the CTF correction, it is necessary to recall the assumptions made in deriving Eqs. (6) and (8). As pointed out before, these equations are linear approximations for a weak-scattering (weak-phase and weak-amplitude) object and as such are unable to account for strong absorption effects, strong phase shifts, or multiple scattering. In the case of frozen-hydrated samples where scattering is dominated by inelastic scattering (Schröder *et al.*, 1990; Angert *et al.*, 1996), it is possible to reduce multiple scattering effects by filtering out electrons that have undergone energy loss. Thus, zero-loss energy filtering not only improves specimen contrast by reducing the incoherent background from single inelastic scattering, but it also reduces the size of nonlinear components in the image. It should be noted, however, that energy

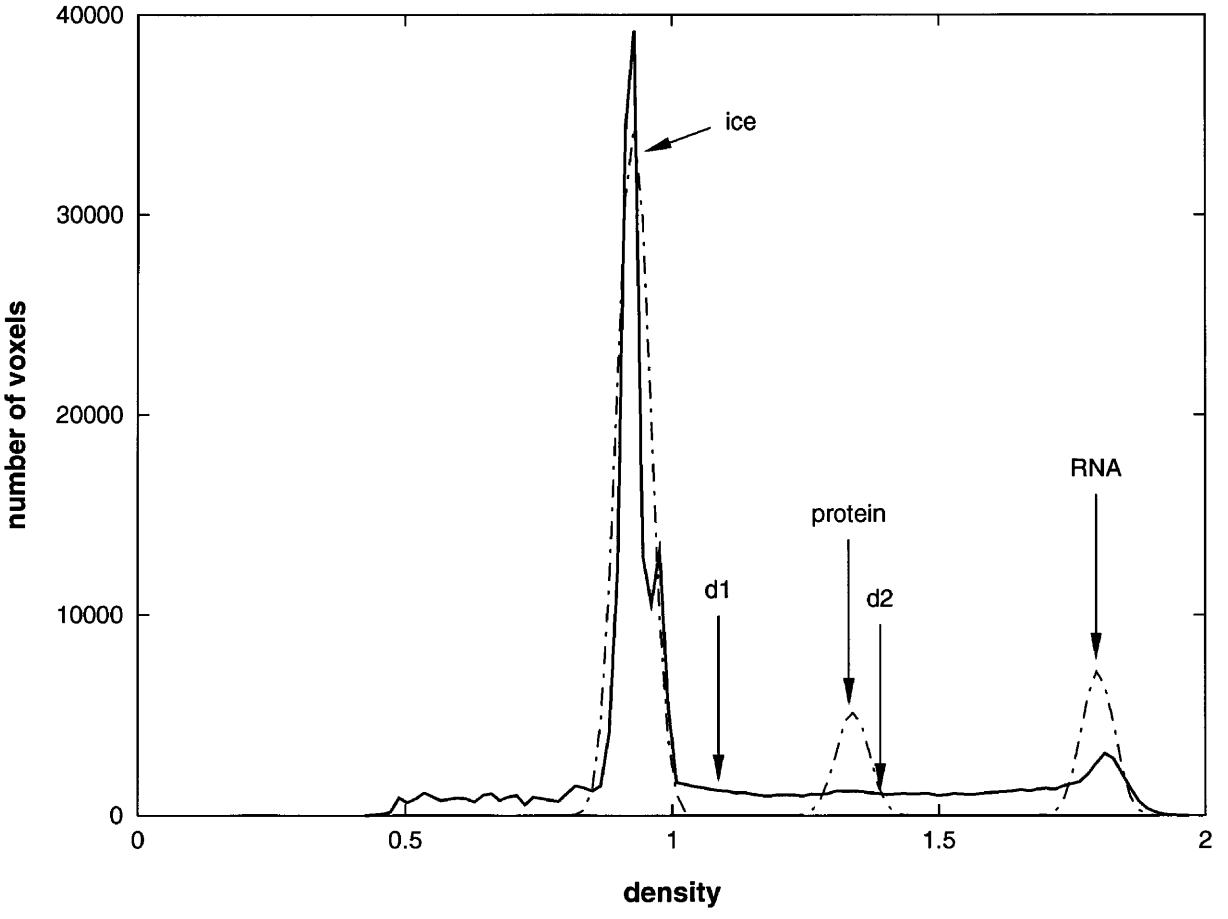

FIG. 11. Histogram of reconstruction from three data sets with and without CTF correction. After CTF correction, the ice peak is sharper and the two peaks become separated more. Solid line: CTF-corrected reconstruction; dashed line: non-CTF-corrected reconstruction. d1 and d2 are density thresholds for volumes of 3.4×10^6 and 2.4×10^6 Å^3 in CTF-corrected reconstruction, respectively.

filtering cannot eliminate electrons that have undergone multiple elastic–elastic scattering, but these form but a small fraction of all electrons participating in image formation for ice thicknesses (600–800 Å) considered here.

An important benefit of energy filtering is that it eliminates all those image components that do not obey the contrast transfer theory and thus makes possible the application of restoration without jeopardizing the accuracy with which low-spatial-frequency components are determined. The immediate result is that external and internal boundaries (channel, tunnels) can be located with much greater fidelity than restored reconstructions from unfiltered data or unrestored reconstructions.

As a side product, our CTF determination procedure has yielded new measurements of the amplitude contrast ratio for biological specimens embedded in ice. We obtain the ratios 0.14 and 0.09 with and without energy filtration, respectively. These values compare favorably with those obtained by Langmore and Smith (1992) (0.14 with energy filtration for a TMV specimen) and Toyoshima and Unwin (1988) (0.07 without energy filtration for an acetylcholine receptor specimen).

The resolution improvement compared with reconstruction from a single-defocus data set is due to an increase in the number of projections and the extension of the useful frequency range beyond the first zero of the CTF by the CTF correction procedure, as discussed under Methods. The resolution at this point is mostly limited by the number of particles and the effects are summarized by envelope $E_g(k)$ (Kenney *et al.*, 1992). Another limitation may come from the particular combination of defocus values we used.

The results imply that further resolution improvement is possible both by addressing instrument instabilities and by adding more particles either from defocus series or from micrographs at random defocus. In future work it will be necessary to find a optimal coverage of defocus values that eliminates

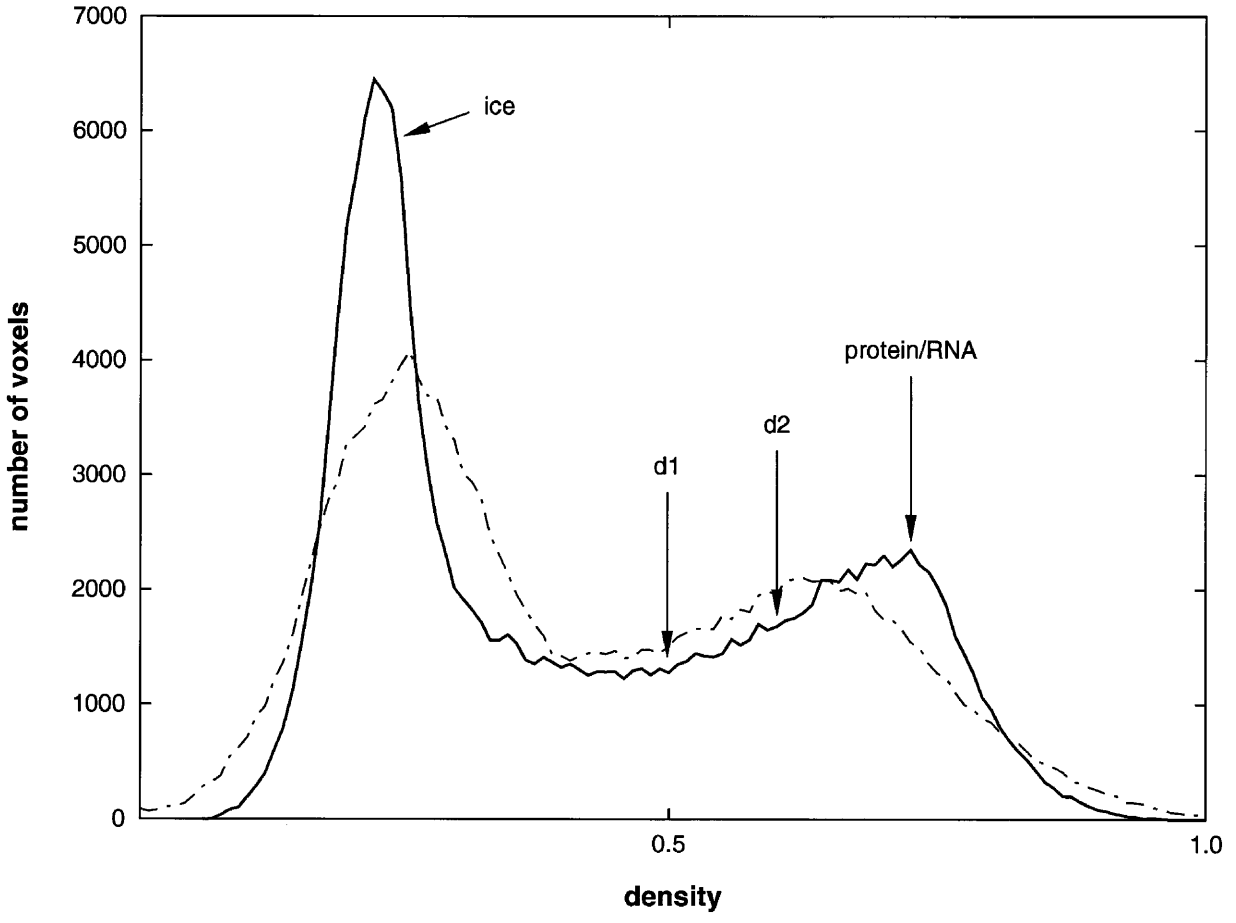

FIG. 12. Histogram of a ribosome density model built from three components: ice, protein, and RNA. Solid line: histogram of the model; dashed line: histogram of low-pass-filtered model. The filter parameters are the same as the low-pass-filtering parameters for all the volumes. After the low-pass filtration, the peak for the protein has spread into a broad range of intermediate density. d1 and d2 are the densities corresponding to the volumes of 2.4×10^6 and 3.4×10^6 Å^3, respectively.

coinciding zeros in the different CTFs. In all these experiments, use of zero-loss energy filtering will allow the structural information to be extracted with highest fidelity, virtually free from interference by image components that are, from the viewpoint of linear transfer theory, ill-behaved.

This work was supported, in part, by Grants NIH 1R01 GM 29169 and NSF BIR 9219043.

Note added in proof. As this article goes into print, a paper by Stark *et al.* (1997) appeared which describes results obtained by cryoelectron microscopy of ribosomes. Contrary to what the authors state, CTF correction is an absolute necessity for assuring the restoration of *low-resolution* spatial frequency components to their correct amplitude, a task that is made difficult by the presence of components in the image stemming from inelastic scattering. The restoration of these components, facilitated by energy filtration, is particularly important in retrieving the correct external and internal molecular boundaries. The authors do show a CTF correction, which, however, has little effect on the appearance of their ribosome model, presumably because all low-resolution spatial frequencies were already eliminated at an earlier stage of the processing.

REFERENCES

Angert, I., Burmester, C., Dinges, C., Rose, H., and Schröder, R. R. (1996) Elastic and inelastic scattering cross-section of amorphous layers of carbon and vitrified ice, *Ultramicroscopy* **63,** 181–192.

Biemond, J., Lagendijk, R. L., and Mersereau, R. M. (1990) Iterative methods for image deblurring. *Proc. IEEE* **78,** 856–883.

Boisset, N., Penczek, P., Pochon, F., Frank, J., and Lamy, J. (1993) Three-dimensional architecture of human α2-macroglobin transformed with methylamine, *J. Mol. Biol.* **232,** 522–529.

Carazo, J. M. (1992) The fidelity of 3D reconstruction from incomplete data and the use of restoration methods, *in* Frank, J. (Ed), Electron Tomography, pp. 117–164, Plenum, New York.

Dinges, C., Berger, A., and Rose, H. (1995) Simulation of TEM images considering phonon and electronic excitations, *Ultramicroscopy* **60,** 49–70.

Downing, K. H., and Grano, D. A. (1982) Analysis of photographic emulsions for electron microscopy of two-dimensional crystalline specimen, *Ultramicroscopy* **7,** 381–404.

Erickson, H. P., and Klug, A. (1970) The Fourier transform of an electron micrograph: Effects of defocussing and aberrations, and implications for the use of underfocus contrast enhancement. *Ber. Bunsenges. Phys. Chem.* **74,** 1129–1137.

Fernandez, J. J., and Carazo, J. M. (1997) A spectral estimation approach to contrast transfer function detection in electron microscopy. *Ultramicroscopy,* in press.

Frank, J. (1973) The envelope of electron microscopic transfer functions for partially coherent illumination, *Optik* **38,** 519–536.

Frank, J., Shimkin, B., and Dowse, H. (1981a) SPIDER-a modular software system for electron image processing, *Ultramicroscopy* **6,** 343–358.

Frank, J., Verschoor, A., and Boublik, M. (1981b) Computer averaging of electron micrographs of 40S ribosomal subunits, *Science* **214,** 1353–1355.

Frank, J., Radermacher, M., Wagenknecht, T., and Verschoor, A. (1988a) Studying ribosome structure by electron microscopy and computer-image processing. *Methods Enzymol.* **164,** 3–35.

Frank, J., Verschoor, A., Wagenknecht, T., Radermacher, M., and Carazo, J. M. (1988b) A new non-crystallographic image-processing technique reveals the architecture of ribosomes, *Trends Biochem. Sci.* **13,** 123–127.

Frank, J. (1990) Classification of macromolecular assemblies studied as 'single particles', *Q. Rev. Biophys.* **23,** 281–329.

Frank, J., Penczek, P., Grassucci, R., and Srivastava, S. (1991) Three-dimensional reconstruction of the 70S *Escherichia coli* ribosome in ice—the distribution of ribosomal RNA, *J. Cell Biol.* **115,** 597–605.

Frank, J., Verschoor, A., Li, Y. H., Zhu, J., Lata, R. K., Radermacher, M., Penczek, P., Grassucci, R., Agrawal, R. K., and Srivastava, S. (1995a) A model of the translational apparatus based on a three-dimensional reconstruction of the *Escherichia coli* ribosome, *Biochem. Cell Biol.* **73,** 757–765.

Frank, J., Zhu, J., Penczek, P., Li, Y., Srivastava, S., Verschoor, A., Grassucci, R., Lata, R. K., and Agrawal, R. K. (1995b) A model of protein synthesis based on cryo-electron microscopy of the *E. coli* ribosome, *Nature* **376,** 441–444.

Frank, J., Radermacher, M., Penczek, P., Zhu, J., Li, Y., Ladjadj, M., and Leith, A. (1995c) SPIDER and WEB: Processing and visualization of images in 3D electron microscopy and related fields, *J. Struct. Biol.* **116,** 190–199.

Frank, J., and Penczek, P. (1995) On the correction of the contrast function in biological electron microscopy, *Optik* **98,** 125–129.

Hanszen, K. J. (1971) The optical transfer theory of the electron microscope: Fundamental principles and applications, *Adv. Opt. Microsc.* **4,** 1–84.

Harris, F. J. (1978) On the use of windows for harmonic analysis with the discrete Fourier transform, *Proc. IEEE* **66,** 51–83.

Kenney, J. M., Hantula, J., Fuller, S. D., Mindich, L., Ojala, P. M., and Bamford, D. H. (1992) Bacteriophage-phi6 envelope elucidated by chemical cross-linking, immunodetection, and cryoelectron microscopy, *Virology* **190,** 635–644.

Kessel, M., Frank, J., and Goldfarb, W. (1980) Averages of glutamine synthetase molecules as obtained with various skin and electron dose conditions, *J. Supramol. Struct.* **14,** 405–422.

Langmore, J. P., and Smith, M. F. (1992) Quantitative energy-filtered electron microscopy of biological molecules in ice, *Ultramicroscopy* **46,** 349–373.

Lepault, J., Booy, F. P., and Dubochet, J. (1983) Electron microscopy of frozen biological suspensions, *J. Microsc.* **129,** 89–102.

Möbus, G., and Rühle, M. (1993) A new procedure for the determination of the chromatic contrast transfer envelope of electron microscopes, *Optik* **93,** 108–118.

Palade, G. E. (1955) A small particulate component of the cytoplasm, *J. Biophys. Biochem. Cytol.* **1,** 59–69.

Penczek, P., Radermacher, M., and Frank, J. (1992) Three-dimensional reconstruction of single particles embedded in ice, *Ultramicroscopy* **40,** 33–53.

Penczek, P. A., Grassucci, R. A., and Frank, J. (1994) The ribosome at improved resolution: new techniques for merging and orientation refinement in 3D cryo-electron microscopy of biological particles, *Ultramicroscopy* **53,** 251–270.

Penczek, P., Zhu, J., and Frank, J. (1996) A common-lines based method for determining orientations for $N > 3$ particle projections simultaneously, *Ultramicroscopy* **53,** 205–218.

Press, W. H., Teukolsky, S. A., Vetterling, W. T., and Flannery, B. P. (1992) Numerical Recipes, 2nd ed, Cambridge Univ. Press, Cambridge.

Radermacher, M., Wagenknecht, T., Verschoor, A., and Frank, J. (1987) Three-dimensional reconstruction from a single-exposure, random conical tilt series applied to the 50S ribosomal subunit of *Escherichia coli, J. Microsc.* **146,** 113–136.

Reimer, L., and Ross-Messemer, M. (1990) Contrast in the electron spectroscopic imaging mode of a TEM, *J. Microsc.* **159,** 143–160.

Schiske, P. (1973) Image processing using additional statistical information about the object, *in* Hawkes, P. W. (Ed.), Image Processing and Computer-aided Design in Electron Optics, pp. 82–90, Academic Press, London.

Schröder, R. R., Hofmann, W., and Menetret, J. F. (1990) Zero-loss energy filtering as improved imaging mode in cryoelectron microscopy of frozen-hydrated specimens, *J. Struct. Biol.* **105,** 28–34.

Schröder, R. R., Manstein, D. J., Jahn, W., Holden, H., Rayment, I., Holmes, K. C., and Spudich, J. A. (1993) Three-dimensional atomic model of F-actin decorated with *Dictyostelium* myosin S1, *Nature* **364,** 171–174.

Schuster, A. (1898) On the investigation of hidden periodicities with application to a supposed 26 days period of meteorological phenomenon, *Terr. Magn.* **3,** 13–41.

Smith, M. F., and Langmore, J. P. (1992) Quantitation of molecular densities by cryo-electron microscopy. Determination of the radial density distribution of tobacco mosaic virus, *J. Mol. Biol.* **226,** 763–774.

Stark, H., Mueller, F., Orlova, E. V., Schatz, M., Dube, P., Erdemir, T., Zemlin, F., Brimacombe, R., and van Heel, M. (1995) The 70S *Escherichia coli* ribosome at 23 Å resolution: Fitting the ribosomal RNA, *Structure* **3,** 815–821.

Stewart, M., and Vigers, G. (1986) Electron microscopy of frozen-hydrated biological material, *Nature* **319,** 631–636.

Toyoshima, C., Yonekura, K., and Sasabe, H. (1993) Contrast transfer for frozen-hydrated specimens II. Amplitude contrast at very low frequencies, *Ultramicroscopy* **48,** 165–176.

Toyoshima, C., and Unwin, P. N. T. (1988) Contrast transfer for frozen-hydrated specimens: determination from pairs of defocus images, *Ultramicroscopy* **25,** 279–292.

Typke, D., Hegerl, R., and Kleinz, J. (1992) Image restoration for biological objects using external TEM control and electronic image recording. *Ultramicroscopy* **46,** 157–173.

Typke, D., and Radermacher, M. (1982) Determination of the phase of complex atomic scattering amplitudes from light-optical diffractograms of electron microscope images, *Ultramicroscopy* **9,** 131–138.

Unwin, P. N. (1977) Three-dimensional model of membrane-bound ribosomes obtained by electron microscopy, *Nature* **269,** 118–122.

van Heel, M. (1987) Angular reconstitution: a posterior assignment of projection directions for 3D reconstruction, *Ultramicroscopy* **21,** 111–124.

Wade, R. H. (1992) A brief look at imaging and contrast transfer, *Ultramicroscopy* **46,** 145–156.

Wade, R. H., and Frank, J. (1977) Electron microscope transfer functions for partially coherent axial illumination and chromatic defocus spread, *Optik* **49,** 81–92.

Wagenknecht, T., Grassucci, R., and Frank, J. (1988) Electron microscopy and computer image averaging of ice-embedded large ribosomal subunits from *Escherichia coli, J. Mol. Biol.* **199,** 137–147.

Welch, P. D. (1967) The use of fast Fourier transform for the estimation of power spectra: A method based on time averaging over short modified periodograms, *IEEE Trans. Audio Electroacoust.* **AU-15,** 70–73.

Wittmann, H. G. (1982) Components of bacterial ribosomes. *Annu. Rev. Biochem.* **51,** 155–183.

Yonath, A., Leonard, K. R., and Wittmann, H. G. (1987) A tunnel in the large ribosomal subunit revealed by three-dimensional image reconstruction, *Science* **236,** 813.

Yonath, A., and Wittmann, H. G. (1988) Challenging the three-dimensional structure of ribosomes, *Biophys. Chem.* **29,** 17.

Zhou, Z. H., and Chiu, W. (1993) Prospects for using an IVEM with a FEG for imaging macromolecules towards atomic resolution, *Ultramicroscopy* **49,** 407–416.